Nanoactuator for Neuronal Optoporation

Marlene E Pfeffer, Mattia Lorenzo Difrancesco, Arin Marchesi, Filippo Galluzzi, Matteo Moschetta, Andrea Rossini, Simona Francia, Clemens M Franz, Yulia Fok, Claire Valotteau, et al.

ACS NANO

www.acsnano.org

ARTICLE

Nanoactuator for Neuronal Optoporation

Marlene E. Pfeffer,[§§] Mattia Lorenzo DiFrancesco,[*,§§] Arin Marchesi, Filippo Galluzzi, Matteo Moschetta, Andrea Rossini, Simona Francia, Clemens M. Franz, Yulia Fok, Claire Valotteau, Giuseppe Maria Paternò, Lorena Redondo Morata, Francesca Vacca, Sara Mattiello, Arianna Magni, Luca Maragliano, Luca Beverina, Giuseppe Mattioli, Guglielmo Lanzani, Pietro Baldelli,[*] Elisabetta Colombo,[§§] and Fabio Benfenati[*,§§]

Cite This: https://doi.org/10.1021/acsnano.4c01672

Read Online

ACCESS | Metrics & More | Article Recommendations | Supporting Information

ABSTRACT: Light-driven modulation of neuronal activity at high spatial-temporal resolution is becoming of high interest in neuroscience. In addition to optogenetics, nongenetic membrane-targeted nanomachines that alter the electrical state of the neuronal membranes are in demand. Here, we engineered and characterized a photoswitchable conjugated compound (BV-1) that spontaneously partitions into the neuronal membrane and undergoes a charge transfer upon light stimulation. The activity of primary neurons is not affected in the dark, whereas millisecond light pulses of cyan light induce a progressive decrease in membrane resistance and an increase in inward current matched to a progressive depolarization and action potential firing. We found that illumination of BV-1 induces oxidation of membrane phospholipids, which is necessary for the electrophysiological effects and is associated with decreased membrane tension and increased membrane fluidity. Time-resolved atomic force microscopy and molecular dynamics simulations performed on planar lipid bilayers revealed that the underlying mechanism is a light-driven formation of pore-like structures across the plasma membrane. Such a phenomenon decreases membrane resistance and increases permeability to monovalent cations, namely, Na^+, mimicking the effects of antifungal polyenes. The same effect on membrane resistance was also observed in nonexcitable cells. When sustained light stimulations are applied, neuronal swelling and death occur. The light-controlled pore-forming properties of BV-1 allow performing "on-demand" light-induced membrane poration to rapidly shift from cell-attached to perforated whole-cell patch-clamp configuration. Administration of BV-1 to *ex vivo* retinal explants or *in vivo* primary visual cortex elicited neuronal firing in response to short trains of light stimuli, followed by activity silencing upon prolonged light stimulations. BV-1 represents a versatile molecular nanomachine whose properties can be exploited to induce either photostimulation or space-specific cell death, depending on the pattern and duration of light stimulation.

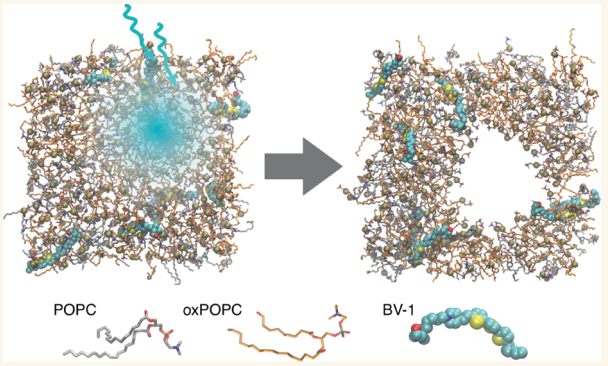

KEYWORDS: *molecular machines, membrane pores, neuronal photostimulation, perforated patch, programmed cell death*

INTRODUCTION

The possibility of modulating neuronal activity and viability using light-sensitive nanotechnological tools is a breakthrough in neuroscience. Optogenetics, expressing light-sensitive actuators to induce depolarizing or hyperpolarizing currents in genetically selected neuronal populations, was a breakthrough, holding noticeable spatial-temporal resolution and specificity in driving and modulating neural activity.[1] As an alternative to optogenetics not implying genetic modifications of target neurons, several groups have generated smart-material nanotools to create light-sensitive abiotic/biotic interfaces with target neural cells. Many of these interfaces exploit the colloidal or water-soluble nature of the light-actuators to fast-track their diffusion in cells and tissues, such as gold nanoparticles, polymeric semiconductor nanoparticles, or upconverting nanoparticles, that are able to induce membrane depolarization driven by infrared or visible light stimuli through heat generation associated with stimulation of TRPV1 channels, activation of transduced microbial opsins, or pseudocapacitive effects.[2−9]

Received: February 3, 2024
Revised: April 5, 2024
Accepted: April 18, 2024
Published: April 30, 2024

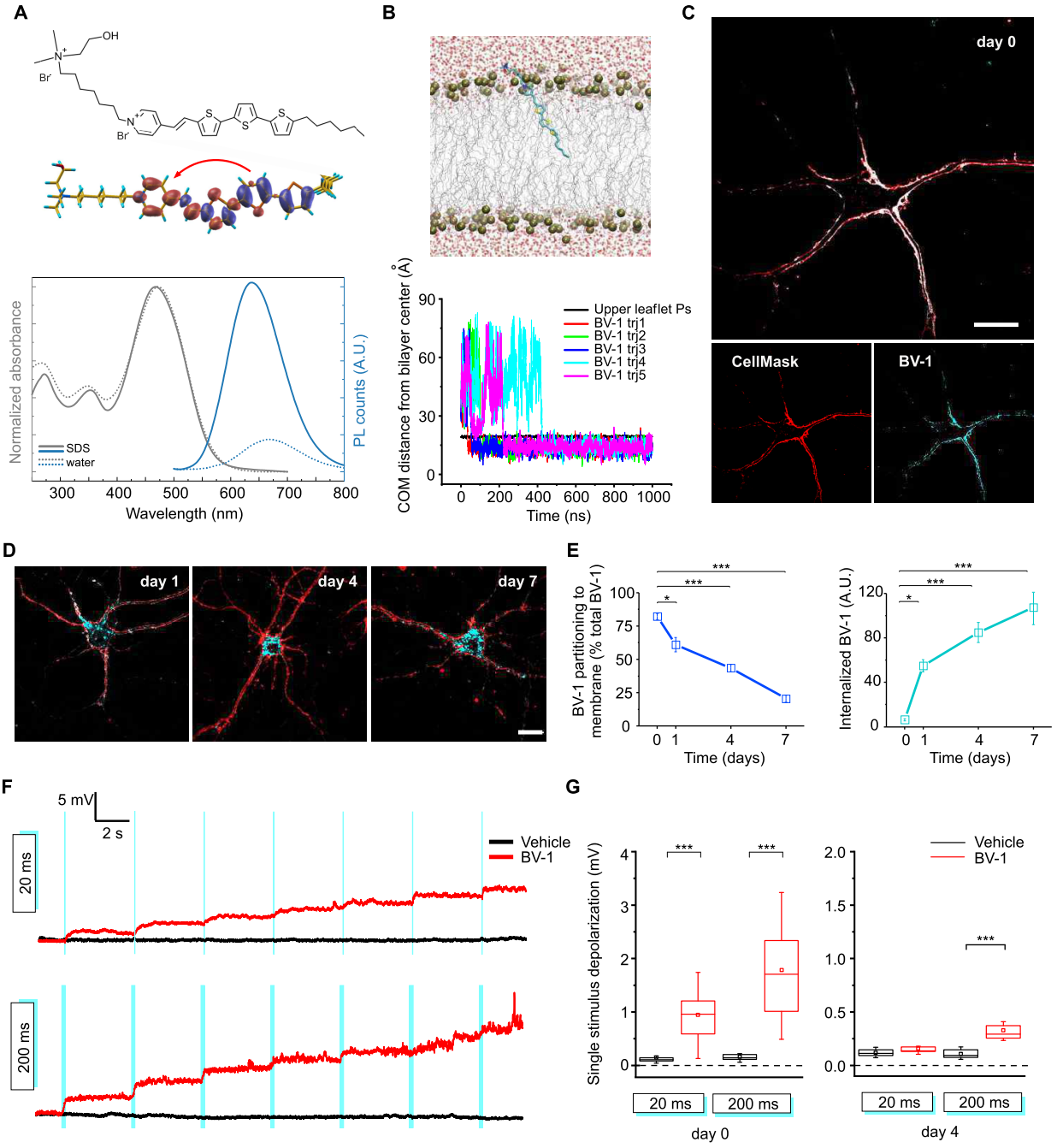

Figure 1. Time-dependent internalization of BV-1 and membrane voltage modulation. (A) The chemical structure of BV-1 and BV-1 optimized geometry with charge density displacement between the ground and first excited state. Blue and red regions indicate charge depletion and accumulation, respectively (upper panel), upon excitation. BV-1 (25 μM) absorbance and photoluminescence spectra in sodium dodecyl sulfate (0.1 μM) and water (lower panel). (B) Molecular Dynamics simulations of BV-1 insertion into the lipid bilayer: a snapshot of the membrane-inserted BV-1 (upper panel) and insertion dynamics (lower panel). (C) Representative confocal images of primary hippocampal neurons acquired after incubation with BV-1 (1 μM) and CellMask (5 μM) for 5 min. Cell membrane stained with CellMask (red) and BV-1 intrinsic fluorescence (cyan). Scale bar, 20 μm. (D) Confocal images taken at 1, 4, and 7 days after a single-pulse incubation with BV-1, showing the progressive internalization of the molecule. Scale bar, 20 μm. (E) Left: Quantification of BV-1 fraction colocalizing with CellMask in percent of the total BV-1 fluorescence (n = 14, 12, 16, and 9 for day 0, day 1, day 4, and day 7, respectively). *Right:* Quantification of the time-dependent internalization of BV-1 (n = 6, 15, 16, and 6 for day 0, day 1, day 4, and day 7, respectively). (F) Representative membrane voltage traces recorded in current-clamp (CC, I_h = 0 pA) in primary hippocampal neurons. Cells were incubated with either vehicle (H_2O, black traces) or BV-1 (1 μM, red traces) and stimulated with subsequent light pulses (470 nm; 3 mW/mm^2) for 20 (upper traces) or 200 (lower traces) ms administered at 0.25 Hz. Recordings were performed at day 0 in the presence of excitatory and inhibitory synaptic blockers. (G) Single-stimulus depolarization calculated in a 300 ms time window from the first light onset and quantified at day 0 (left panel) and day 4 (right panel) after a single-pulse incubation with either Vehicle (black boxes) or BV-1 (red boxes). Day 0: n = 13 and 16; day 4: n = 8 and 13 for Vehicle and BV-1, respectively. Statistics: *p < 0.05, ***p < 0.001; Kruskal–Wallis/Dunn's tests (E); unpaired Student's t-test/Mann–Whitney's U-test (G).

https://doi.org/10.1021/acsnano.4c01672
ACS Nano XXXX, XXX, XXX–XXX

An alternative strategy is the engineering of membrane-targeted photoswitches that undergo light-induced isomerization.[10,11] Initially, UV-sensitive tethered photoswitches covalently linked to recombinant ligand-gated or voltage-gated ion channels allowed modulating ion channel dynamics and/or the electrical properties of the membrane in a light-dependent manner.[12] More recently, azobenzene-based photoswitchable affinity labels were shown to photosensitize endogenous proteins without the requirement of genetic engineering. A first class of such probes in which the azobenzene group was flanked by quaternary ammonium proved to be effective in blocking K^+- and HCN-channels in response to UV light, thereby triggering neuronal activation in both primary neurons and retinal explants.[13,14] From the original probe, photoswitches sensitive to visible light and triggering light-reversible blockade of voltage- or ligand-gated ion channels have been generated.[15−17] Recently, we have engineered an amphiphilic azobenzene-based photoswitch, named Ziapin, that acts as an intramembrane actuator for inducing reversible membrane capacitance perturbation upon irradiation with visible light.[18,19] Photochromic molecules therefore represent a biomimetic tool acting directly on membrane properties upon illumination that minimizes any interference with the physiological environment and the consequent risk of undesired side effects.

Several physical, chemical, microbic, or immune mechanisms can induce membrane damage and poration, potentially leading to cell death. In addition to these stressors, endogenously regulated cell death mechanisms involving membrane breaching by specialized pore-forming proteins or polycationic molecules exist and play an important role in tissue defense from infections and in cell turnover.[20,21] Membrane poration can also be achieved using molecular motors/switches engineered to produce nanomechanical actions on the plasma membrane triggered by adequate stimuli.[22,23] In addition to these molecular technologies, light-driven nanotechnology has also been applied to induce membrane poration with high precision and low invasiveness, leading to diverse applications from drug and gene delivery to targeted cell death.[24,25] Laser-assisted optoporation is an efficient tool for loading cells with large molecules such as cDNA or small beads,[26,27] and its throughput can be enhanced by nanosensitizers and nanostructures.[28−30] In this respect, plasmonic optoporation on three-dimensional (3D) microelectrode arrays was recently shown to open transient nanopores in cell membranes without compromising the seal between the cell membrane and the nanoelectrode.[31]

Here, we synthesized and characterized a membrane-targeted photoswitchable conjugated compound (BV-1) that combines, in one versatile nanodiagnostic/nanotherapeutic tool, the neuronal modulation capabilities of photoisomerizable substances with the on-demand poration of the cell membrane. We show that BV-1 spontaneously partitions into the neuronal membrane and does not interfere with neuronal viability and activity in the dark. Upon millisecond light pulses in the cyan region of the spectrum, a short-lived charge transfer within the compound triggers an irreversible supramolecular process in the membrane environment that results in the formation of pore-like structures in the lipid bilayer. We found that the pore formation is due to light-triggered oxidation of membrane phospholipids by BV-1 that decreases membrane tension and increases membrane fluidity. A cumulative depolarization and action potential firing are observed with a progressive impairment of voltage-dependent currents. Thanks to these light-dependent properties, we also show that BV-1 allows light-controlled perforated patch-clamp configuration in the presence of the compound in the recording pipet. As the pore-forming process triggered by light is not reversible, neuronal swelling and death can be induced upon prolonged light stimulation. *Ex vivo* treatment of blind retinal explants with BV-1 or in vivo stereotaxic injection of BV-1 into the primary visual cortex revealed the ability of the compound to induce neuronal stimulation or neuronal activity silencing and death in response to short-lived or prolonged light stimulation, respectively. Thanks to its multifunctional properties, BV-1 represents a versatile molecular compound with photoswitchable activity that can be exploited for a range of biological effects, from neuronal photostimulation to space-specific cell death, by tuning patterns and duration of light stimulation.

RESULTS

BV-1 Spontaneously Partitions into a Lipid Bilayer and Induces a Sustained Depolarization. BV-1 is a closed shell dication bearing positively charged alkyl-ammonium and *N*-alkyl-pyridinium moieties. The synthesis of the compound is described in detail in the Supplementary Methods. The electron-deficient pyridinium block is connected to an electron-rich terthiophene block through a conjugated *trans* double bond, resulting in the optimized large, planar structure shown in Figure 1A. The molecule is characterized by a highest occupied molecular orbital (HOMO) orbital mainly localized on the terthiophene block and a lowest unoccupied molecular orbital (LUMO) orbital centered on the pyridinium cation (Figure S1). These electronic properties of the ground state are, in turn, responsible for optical properties, with the calculated absorption spectrum of BV-1 dominated by a strong S0 → S1 transition in the visible spectrum, almost entirely assigned (94%) to a single particle HOMO−LUMO excitation and peaking at 478 nm (Figure S1), in agreement with the experimentally measured spectra (Figure 1A, lower panel). The upper panel of Figure 1A also shows the charge density difference between the ground state S0 and the S1 excited state, with the charge density displaced from blue to red regions. Such displacement clearly indicates the nature of S1 as a charge-transfer state, with a charge depletion from thiophene units and a charge accumulation mainly involving the pyridinium ring (Figure 1A; blue and red regions, respectively). By comparing the absorption and emission spectra of BV-1 in water or in detergent (sodium dodecyl sulfate, SDS) micelles mimicking the environment of the membrane, we observed an ∼50 nm blue shift of BV-1 emission associated with a noticeable increase in the emission quantum yield in SDS, suggesting that the molecule may spontaneously partition into the plasma membrane by virtue of its amphiphilicity (Figure 1A, lower panel).

To investigate the spontaneous insertion of BV-1 in the membrane, we performed five independent, 1 μs-long molecular dynamics (MD) simulations of one BV-1 molecule in the dark state placed at random orientations in bulk water in the proximity of a 1-palmitoyl-2-oleoyl-phosphatidylcholine (POPC) double-layer. In all cases, BV-1 entered the bilayer within 500 ns by first inserting the thiophene-containing side and remained in the membrane for the rest of the trajectory, with its main axis nearly parallel to the bilayer normal (Figure 1B). In this stable conformation, the positively charged alkyl-

https://doi.org/10.1021/acsnano.4c01672
ACS Nano XXXX, XXX, XXX−XXX

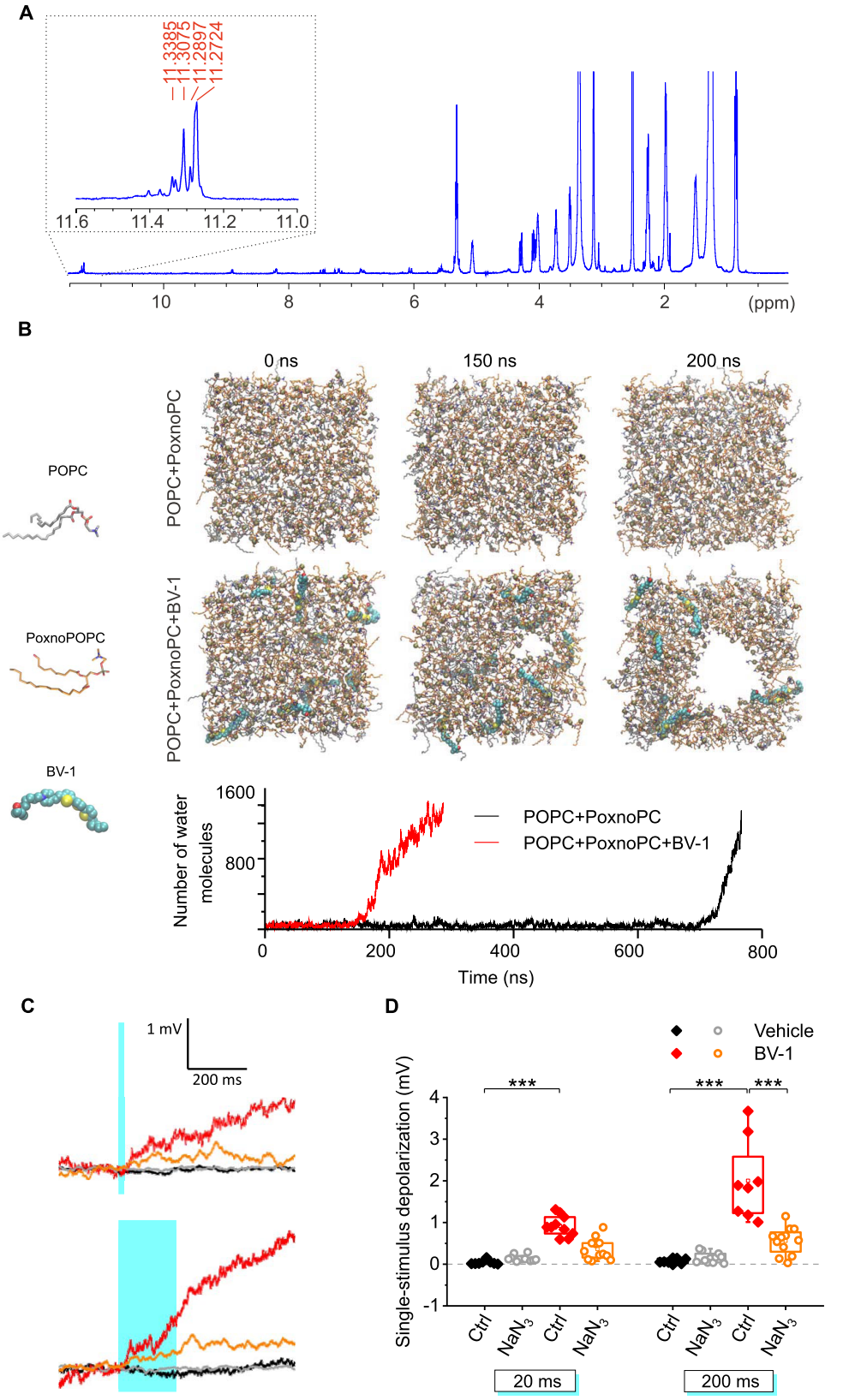

Figure 2. Irradiation of BV-1 induces lipid oxidation that greatly increases the propensity of the membrane to form spontaneous pores. (A) The ^{1}H NMR spectrum (DMSO-d_6) of a DOPC/choline 1:1 (mol:mol) mixture after 5 min irradiation as a 0.20 mg/mL aqueous solution at 365 nm under a TLC UV-lamp in the presence of a 50 μM concentration of BV-1. The inset shows a zoom of the 11.5−11.0 ppm region featuring the signals attributed to the carboxylic acid functionalities produced by oxidation of the lipids. (B) Top: Snapshots extracted from simulations of a solvated membrane composed of a 2:1 ratio of PoxnoPC (an oxidation product of POPC) and POPC lipids, without (upper row) and with (lower row) BV-1 inserted. Lipid phosphorus atoms are represented as bronze spheres. PoxnoPC carbon atoms are colored in orange, while those of POPC are colored in gray. BV-1 atoms are represented as cyan (carbon), yellow (sulfur), and red (oxygen) spheres.

https://doi.org/10.1021/acsnano.4c01672
ACS Nano XXXX, XXX, XXX−XXX

Figure 2. continued

Water molecules are not shown for clarity. Bottom: Time evolution of the number of water molecules in the interior of the bilayer in the simulations of PoxnoPC/POPC systems in the absence (black line) or presence of BV-1 (red line). (C, D) Inhibition of light-evoked depolarization by pretreatment with sodium azide (1 μg/mL NaN_3; 60 min). (C) Voltage traces recorded in current-clamp from primary hippocampal neurons incubated with vehicle (black), NaN_3 (gray), vehicle + BV-1 (red), or NaN_3 + BV-1 (yellow) and stimulated with either 20 or 200 ms light stimulation (upper and lower traces, respectively). (D) Single-stimulus depolarization calculated in a 300 ms time window from the light onset. Statistics: ***$p < 0.001$; one-way Kruskal–Wallis ANOVA/Dunn's tests within "20 ms" and "200 ms" groups (n = 8, 11, 10, 12, 8, 11, 8, 12, respectively).

ammonium group is at the level of the phospholipid heads, interacting with phospholipid phosphate groups.

To confirm the prediction of BV-1 spontaneous insertion into the cellular membrane, we loaded BV-1 in the extracellular medium of primary hippocampal neurons and investigated its colocalization with the cell membrane marker CellMask (Figure 1C). After 5 min of incubation, approximately 80% of the molecule colocalized with CellMask, confirming the MD predictions. The compound followed the physiological membrane turnover and displayed a progressive time-dependent internalization over time after the initial pulse incubation, with a progressive decrease in surface localization (~52% at day 4 compared to day 0; Figure 1D,E).

To study the effects of BV-1 on neuronal physiology, we performed whole-cell patch-clamp recordings of primary hippocampal neurons loaded with the compound and either kept in the dark or subjected to light pulses at 470 nm corresponding to the BV-1 peak absorbance (Figure 1F). Membrane incorporation of BV-1 in the dark did not alter the neuronal membrane potential with respect to the vehicle (see also Figure 3B). However, upon either 20 or 200 ms light pulses (3 mW/mm^2) administered at 0.25 Hz, a stepwise depolarization was observed after each stimulus, highlighting the correlation between light stimulus duration and magnitude of depolarization (Figure 1G, left). Four days after incubation, a smaller, but still significant, depolarization was observed in neurons upon 200 ms light stimulation, while no significant responses were detected in response to 20 ms pulses (Figure S2; Figure 1G, right). The reduced efficacy over time from the initial administration of the compound correlates with the progressive decrease of plasma membrane BV-1 due to membrane trafficking and internalization (see Figure 1D,E). The proportionally smaller depolarization at day 4 (19% depolarization compared to day 0) with respect to the decrease in the membrane concentration of BV-1 suggests that the light-dependent effect might be attributed to a cooperative interaction between several BV-1 molecules.

BV-1 Induces Photo-Oxidation of Membrane Phospholipids that Increases the Propensity for Pore Formation. Since it was recently shown that BV-1, within a hydrophobic environment, can transfer energy to molecular oxygen upon illumination, producing singlet oxygen, we addressed the possibility that light stimulation of membrane-embedded BV-1 induces oxidative decomposition of membrane phospholipids.[32,33] A 1:1 mixture of DOPC/choline, irradiated in the presence of BV-1 (50 μM), showed the characteristic ^{1}H NMR spectral features of carboxylic acid functionalities produced by oxidation of the lipids, observed in the 11.5–11.0 ppm region (Figure 2A), as it could be expected from the cleavage of double bonds by singlet oxygen.

Since phospholipid oxidation above a given threshold is known to profoundly alter the membrane's biophysical properties and lead to the spontaneous formation of water-permeable pores,[34−36] we performed MD simulations of a solvated membrane composed of a 2:1 ratio of PoxnoPC (an oxidation product of POPC) and POPC lipids and observed spontaneous pore formation after 600 ns. Interestingly, the presence of BV-1 in light-activated conformation greatly enhanced the formation of a water-permeable pore in the same system, which appeared at about 150 ns and progressively enlarged thereafter (Figure 2B). This indicates that the oxidation of phospholipids by light-activated BV-1 is the mechanism underlying the spontaneous membrane poration that causes the progressive membrane depolarization observed in primary neurons (see Figure 1F,G). Moreover, the presence of BV-1 within the lipid bilayer greatly accelerates the poration effect of phospholipid oxidation. To further confirm that lipid oxidation is the underlying mechanism, we pretreated neurons with the well-known and potent antioxidant agent, sodium azide, in the absence or presence of BV-1. Interestingly, when light stimulation was applied, a significant depolarization was only observed in neurons treated with the vehicle, while the effect was virtually suppressed in the presence of sodium azide (Figure 2C,D).

We also looked at whether light stimulation changed the distribution of the photoswitchable compound immersed in membrane bilayers by performing two independent, 2 μs-long MD simulations of eight BV-1 molecules in the dark- or light-stimulated state. Results showed that, while in the dark state, the BV-1 molecules remained separate, and after light stimulation, they tended to cluster. This is revealed by the different radial distribution functions of the sulfur atoms from the central thiophene rings, which show no feature for the molecules in the dark state and a marked peak at about 5 Å for the excited ones (Figure S3A). The light-induced clustering of BV-1 molecules, exemplified in the two snapshots extracted at the end of the dark- and light-stimulated simulations (Figure S3B), might enhance the photooxidative effect of BV-1 and concentrate it in discrete membrane spots, generating pores.

Light-Triggered Oxidation of Membrane Phospholipids by BV-1 is Associated with Decreased Membrane Tension and Rigidity and Increased Membrane Fluidity. Given the effects on membrane phospholipids, we further investigated the biophysical characteristics of phospholipid bilayers containing BV-1 and subjected to light stimulation. We first labeled 1:1 phospholipid/cholesterol bilayers with the fluorescent phospholipid dye Texas Red-DHPE and performed fluorescence recovery after photobleaching (FRAP) experiments to determine the kinetics of the two-dimensional lateral diffusion of the unbleached dye to refill the bleached spot (Figure 3A).

After bleaching, control membranes and membranes containing BV-1 kept in the dark had similar behavior in terms of recovery rate and mobile fraction. Strikingly, membrane bilayers incubated with BV-1 and subjected to light stimulation exhibited significant increases in the speed

https://doi.org/10.1021/acsnano.4c01672
ACS Nano XXXX, XXX, XXX−XXX

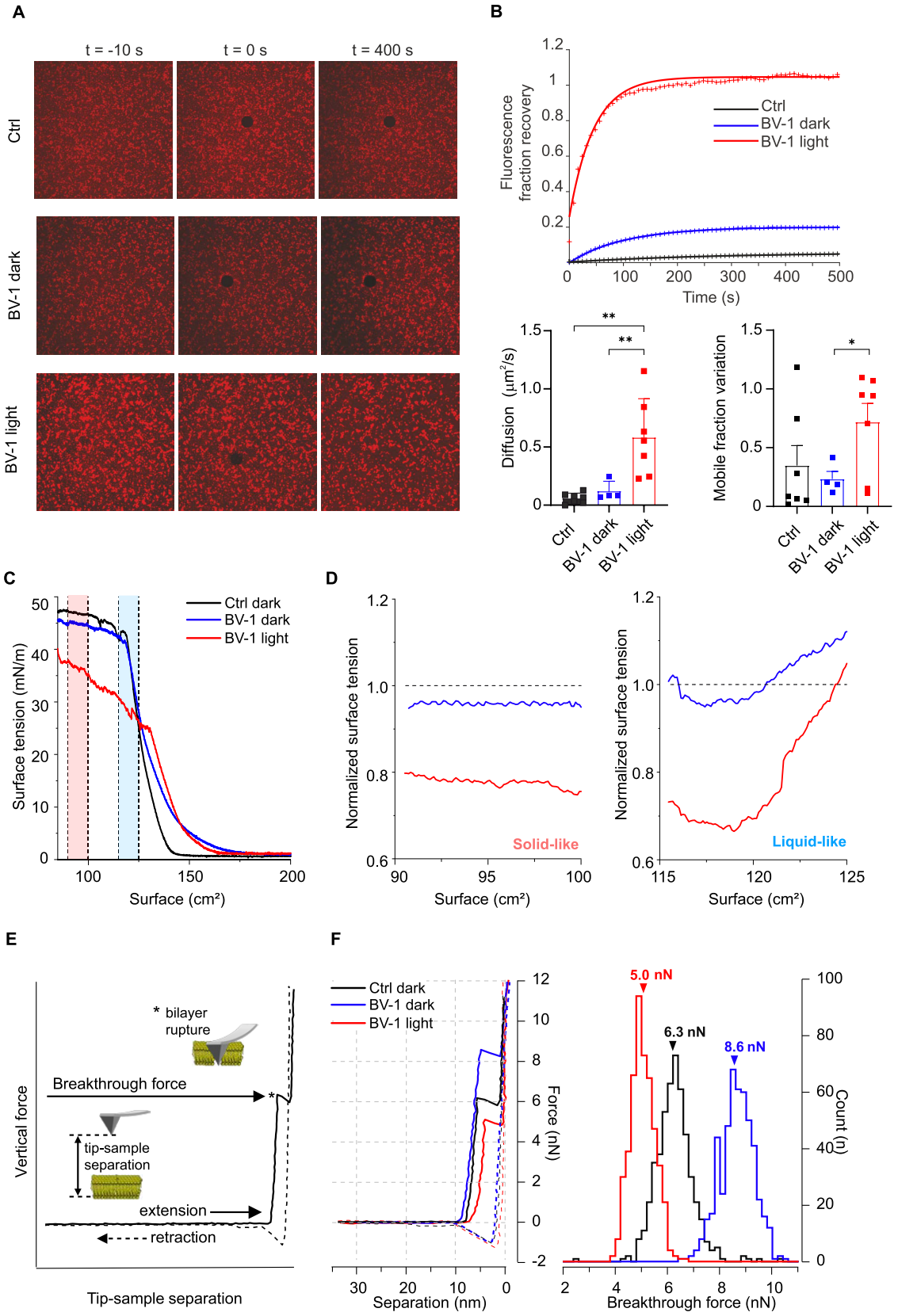

Figure 3. Light stimulation of BV-1 increases membrane fluidity and decreases membrane tension and rigidity. (A) Representative images of POPC:DOPS:cholesterol:Texas Red-DHPE bilayers subjected to the FRAP protocol (bleaching spot 15 μm diameter) 10 s before (t = −10 s), just bleached (t = 0 s), and 400 s after the bleaching procedure. Samples were first recorded under basal conditions; then, membranes were incubated with BV-1 (50 μM; 15 min) in the dark and recorded again; finally, samples were irradiated with cyan light (9 mW/mm²) for 150 s and recorded for the third time. BV-1 illuminated samples show a faster fluorescence recovery if compared to BV-1-treated samples in the dark or untreated control membranes. (B) Top: Fluorescence recovery traces of the bleached ROI normalized with an equal diameter

https://doi.org/10.1021/acsnano.4c01672
ACS Nano XXXX, XXX, XXX−XXX

Figure 3. continued

ROI outside of the bleaching spot. BV-1 illuminated samples show a greater and faster fluorescence recovery compared to BV-1 samples in the dark or control samples. Bottom: Fluorescence traces were fitted with a monoexponential function to yield the time constant used to calculate the diffusion coefficient and the change in mobile fraction. *$p < 0.05$; **$p < 0.01$; one-way analysis of variance (ANOVA)/Bonferroni's tests ($n = 3$ independent preparations). (C, D) Langmuir−Blodgett assay. (C) Changes in surface tension of POPC/cholesterol (1:1) bilayers that were either untreated (Ctrl; black trace) or treated with BV-1 in the dark (blue trace) and after light stimulation (red trace). The red and blue areas indicate the solid-like and liquid-like intervals, respectively. (D) The same curves shown in C were normalized by the values of control bilayers under conditions of solid-like (left) and liquid-like (right). (E, F) Membrane breakthrough assays. (E) Schematics of a typical atomic force microscopy (AFM) indentation experiment with the representative Force−Distance curve for a sample of POPC. The breakthrough is marked with a black dot. (F) Left: Representative breakthrough curves of POPC/cholesterol (1:1) bilayers that were either untreated (Ctrl; black trace) or treated with BV-1 in the dark (blue trace) and after light stimulation (red trace). Right: Histograms of the breakthrough forces for the three experimental groups. A marked decrease in membrane stability is observed upon illumination of BV-1-containing bilayers ($n = 3$ independent experiments).

and extent of fluorescence recovery, diffusion coefficient, and mobile fraction with respect to the dark condition, testifying a marked increase in membrane fluidity upon activation of BV-1 (Figure 3B).

Given the marked increase in membrane fluidity, we investigated to what extent light-activated BV-1 was affecting membrane surface tension, decreasing the threshold for membrane poration. POPC/cholesterol (1:1) bilayers were assessed by the Langmuir−Blodgett method[37] in the presence or absence of BV-1 under dark and light stimulation conditions (Figure 3C). The results show that BV-1 did not markedly affect the surface tension with respect to control bilayers in the dark. However, when activated by light, it induced a dramatic decrease in surface tension, particularly in the areas of maximum membrane compactness (between 90 and 100 cm^2; solid-like), while in the less compact areas (115−125 cm^2; liquid-like), the change in tension due to activated BV-1 progressively decreased (Figure 3D).

To further assess the membrane's biophysical properties in the presence of activated BV-1, we conducted breakthrough experiments by atomic force microscopy (AFM) of POPC/cholesterol (1:1) bilayers in the absence or presence of BV-1 under dark and light stimulation conditions (Figure 3E;[38]). The incorporation of BV-1 into the bilayer in the dark slightly increased membrane rigidity, bringing the average breakthrough force from 6.3 nN of control membranes to 8.6 nN. Illumination of BV-1 promoted a sharp decrease in membrane rigidity, dropping the average breakthrough force from 8.63 to 5.1 nN (Figure 3F). Interestingly, these measurements are also suggestive of a ∼1 nm reduction in bilayer thickness upon irradiation of BV-1-treated membranes, as evidenced by the decreased tip−sample separation at which membrane rupture occurred after illumination (Figure 3F, left panel).

BV-1 Forms Pores in the Lipid Bilayer in a Light-Dependent Manner. To study the consequences of the light-dependent BV-1 aggregation within the cell and visualize the bilayer morphological properties at the nanoscale, we added BV-1 to mica-supported POPC/cholesterol (1:1) bilayers and applied a prolonged light stimulus while continuously imaging the membrane by high-speed AFM (HS-AFM; Figure 4A).

We captured an irreversible lipid fusion (Supplementary Video 1) and a significant reduction in membrane thickness upon light stimulation, as documented by cross-sectional analysis along the dashed lines (Figure 4A, bottom). These observations further corroborate the results reported in FRAP and AFM indentation measurements (see Figure 3), which indicated an increase in bilayer fluidity and a reduction in nanomechanical stability and membrane height upon BV-1 irradiation. Indeed, the time-lapse AFM analysis of the height of the membrane patches above the mica plane shows a clear reduction upon light stimulation (Figure 4B). More specifically, we could appreciate a marked change in the height distribution between t_1 = 126 s (black trace) and t_5 = 932 s (blue trace), with a decrease in the bilayer height from 4.9 to 4.1 nm, respectively (Figure 4C). To further investigate the membrane morphological changes, we focused our HS-AFM imaging over the lipid bilayer plane and observed the formation of nanometric membrane depressions, consistent with the formation of membrane pores by BV-1 upon light stimulation (Figure 4D; Supplementary Video 2), which resulted in an irreversible increase of membrane roughness from ∼0.12 to ∼0.17 nm upon illumination (Figure 4E). These observations were also confirmed through patch-clamp experiments of primary neurons in the cell-attached configuration, where extra-large pore-opening events appeared in BV-1-treated neurons upon light stimulation, superimposed to physiological K^+ single-channel currents (Figure S4).

Light Stimulation of BV-1-Treated Neurons Alters Their Passive Membrane Properties and Generates Na^+-Dependent Inward Currents. We first investigated the changes in membrane resistance evoked by a series of light pulse stimulations (200 ms, 3 mW/mm^2, 2 Hz) by measuring the depolarization slopes induced by inward current ramps (Figure 5A). We observed that membrane resistance of BV-1-treated neurons was not affected in the dark while, upon successive cycles of light stimulation, it exhibited a significant and progressive decrease after each cycle of light stimulation, compatible with a light-dependent opening of membrane pores observed in lipid bilayers (Figure 5B).

To further characterize the light-dependent membrane depolarization, we focused on the modulation of subthreshold neuronal properties and current-clamped neurons at a holding membrane voltage of −70 mV in the presence of blockers of excitatory and inhibitory synaptic transmission and tetrodotoxin (TTX) to block voltage-dependent Na^+ channels and action potential (AP) firing (Figure 5C). Under these conditions, neurons incubated with BV-1 and stimulated with a 30-s train of light pulses (20 ms, 3 mW/mm^2, 1 Hz) experienced a cumulative depolarization of 3.5 ± 0.5 mV associated with an evoked inward current of −17.8 ± 4.3 pA with respect to vehicle (−0.03 ± 0.22 mV and −1.2 ± 0.9 pA, respectively; Figure 5D).

To investigate whether the light-evoked inward current involved Na^+ ions, we repeated the same experimental protocol described above by replacing external Na^+ with an equal concentration of choline (see Methods; Figure 5E). Under

https://doi.org/10.1021/acsnano.4c01672
ACS Nano XXXX, XXX, XXX−XXX

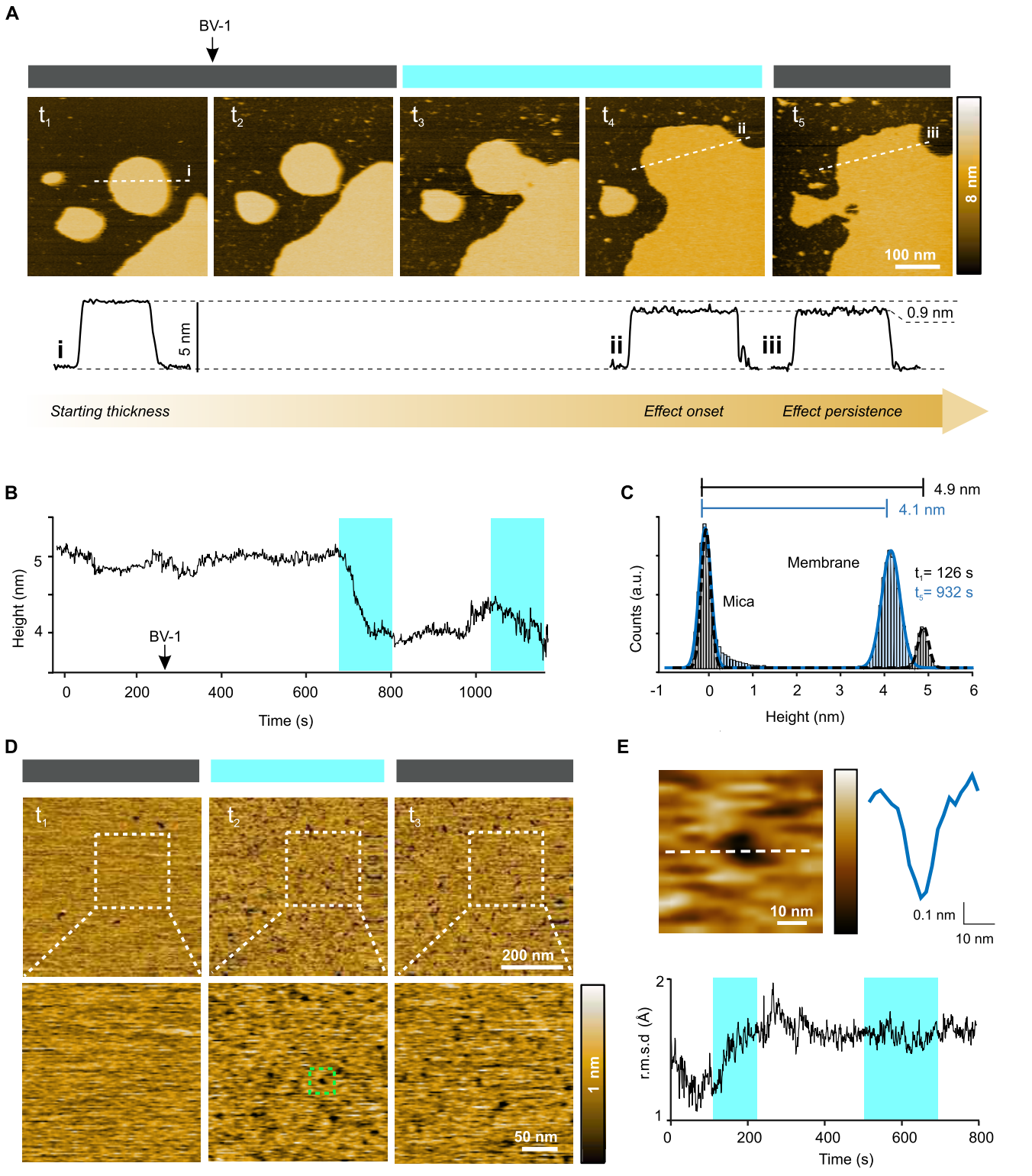

Figure 4. BV-1 triggers thinning and formation of pores in planar lipid bilayers. (A) Time-resolved AFM topographies of POPC/chol = 1:1 (mol:mol) mica-supported membrane dynamics imaged at 1 frame per second at 5 representative time points of the experimental protocol (t_1 = 126 s, t_2 = 667 s, t_3 = 688 s, t_4 = 791 s, t_5 = 932 s, Supplementary Video 1). BV-1 was added in the fluid chamber at a final concentration of 50 μM and allowed to partition into the bilayer for ~7 min. HS-AFM recordings captured irreversible lipid fusion and reduction in membrane thickness upon cyan light irradiation, as documented by the cross-sectional analysis along the dashed lines (i–iii, lower panels). (B) Time-lapse analysis of the height of the membrane patches above the mica plane (Supplementary Video 1). Each data point is the difference between the means of the height distribution of the membrane- and the mica-associated Gaussian components (see panels A and C). (C) Height distributions of the bilayers shown at t_1 (black) and t_5 (blue). For both times, the distributions segregate into two well-resolved peaks separating mica and lipid bilayer height distributions. The two peaks were fitted with the sum of two Gaussian functions. An ~0.8 nm reduction in membrane thickness was observed upon illumination. (D) Time-resolved topographies of the POPC/chol = 1:1 (mol:mol) planar membrane imaged at 1 frame per second at 3 representative time points of the experimental protocol (t_1 = 45 s, t_2 = 211 s,

https://doi.org/10.1021/acsnano.4c01672
ACS Nano XXXX, XXX, XXX–XXX

Figure 4. continued

t_3 = 434 s, Supplementary Video 2) in the presence of 50 μM BV-1 (incubated for about 15 min prior to imaging). HS-AFM recording captured the dynamic formation of nanometric membrane depressions or pores upon cyan light irradiation, only resolved upon tight contrast adjustment on the membrane plane. Enlargements of the white boxed area highlighting the dynamic membrane defects are shown at the bottom of each corresponding frame. (E) Top: Zoom-in of a depression in the BV-1-treated bilayer highlighted in panel E (green box) and the corresponding depth profile. Bottom: Time-lapse analysis of the membrane surface roughness defined as the bilayer r.m.s.d. (see Supplementary Video 2). Pore formation results in an irreversible increase of membrane roughness from ∼0.12 to ∼0.17 nm upon illumination.

these conditions, both the light-evoked depolarization and the light-evoked inward current were markedly decreased (light-evoked membrane depolarization: 1.5 ± 0.6 vs 3.5 ± 0.6 mV in the presence of Na^+; light-evoked inward current −8.7 ± 4.5 vs −17.8 ± 4.3 pA in the presence of Na^+) so that the effects of light stimulation on BV-1-treated neurons became non-significant (Figure 5F). These results support a key role of Na^+ influx in mediating the effects of photostimulation.

To ascertain whether the progressive light-induced depolarization was reversible in the dark, we decreased the concentration of BV-1 to 0.1 μM and varied the duration of light pulses from 20 ms to 3 s (Figure S5, left). At the 10-fold lower BV-1 concentration used, depolarization became significant at pulses of 100 ms or longer and was proportional to the duration of light stimuli. However, membrane voltage failed to return to basal levels at the end of the 8-s protocol, suggesting a substantial irreversibility of the light-triggered membrane depolarization (Figure S5, right).

Firing of Action Potentials is Affected by Light Stimulation in BV-1-Treated Neurons. To assess a possible modulation of neuronal firing, we current-clamped neurons incubated with BV-1, holding the membrane voltage at subthreshold levels (−40 mV) in the presence of synaptic blockers (Figure 6A). Under this condition, similar spontaneous firing activity could be observed in the dark in both vehicle- and BV-1-loaded neurons. However, only BV-1-loaded neurons responded to a train of light stimuli (20 ms, 1 Hz, 3 mW/mm^2) with a progressive depolarization (Figure 6B, left) that, in the absence of TTX, evoked a significant increase of action potential (AP) firing (Figure 6B, right). Interestingly, during the light train, the AP shape progressively changed (Figure 6C). To study the light-induced changes in the AP waveform quantitatively, we used the phase-plane plot analysis to compare the recordings in the dark and at three time points during the light stimulation protocol (Figure 6D). After a few stimulation pulses, the duration of APs increased and, along the stimulation protocol, the AP waveform started displaying an after-spike plateau slightly below 0 mV, often populated by repetitive spikelets. Although individual neurons responded with different dynamics (Figure 6E), virtually all BV-1-treated cells exhibited a clear-cut and progressive increase in the AP half-width with marked slowdown of both rising and repolarizing slopes and decreased AP peak amplitude at the end of the light train stimulation (Figure 6F).

The very same effects of BV-1 on neuronal excitability shown for isolated individual neurons were fully replicated in synaptically active neuronal networks, whose firing activity in response to illumination was extracellularly recorded by multielectrode arrays (MEA) electrophysiology (Figure 6G,H). Primary networks incubated with either vehicle or BV-1 were recorded in the dark before being subjected to a train of pulsed light stimuli lasting 120 s. The average firing rate steadily increased upon illumination, reaching a peak 4-fold the basal activity in about 20 s after the onset of stimulation, to progressively decrease at longer times and drop below the basal activity after 90 s of light stimulation (Figure 6G). Analysis of the AP waveforms recorded extracellularly confirmed the significant widening of the AP that was apparent in the late phase of light stimulation (Figure 6H).

Since the main contributions to the AP shape are voltage-dependent Na^+ and K^+ currents, we investigated the modulation of their conductances under illumination. Vehicle- and BV-1-treated neurons were patch-clamped in the voltage-clamp configuration under conditions to isolate Na^+ and K^+ currents (see Methods) and subjected to light stimulation (20 ms pulse/voltage step).

While in vehicle-treated neurons, no changes in the Na^+ current were observed between dark and light conditions, BV-1-loaded neurons subjected to light stimulation exhibited a slight decrease in the Na^+ current amplitude that was accompanied by a highly significant increase in the time constant of the current decay (Figure S6A). Analysis of the I/V relationship in neurons treated with BV-1 revealed a slight but consistent decrease in Na^+ current amplitude in the voltage range −10/+20 mV induced by light stimulation, while the I/V curve of vehicle-treated neurons was unchanged (Figure S6B).

When K^+ currents were investigated, BV-1-loaded neurons experienced a significant decrease in the K^+ current amplitude in response to light stimulation (Figure S7A). In neurons treated with BV-1, the I/V relationship displayed a light-dependent decrease in current amplitude along the whole voltage range upon light stimulation, while vehicle-treated neurons were insensitive to light pulses (Figure S7B). These observations are in line with the marked and progressive changes in AP shape observed over repetitive light stimulation.

Membrane Permeabilization to Na^+ Ions and Cell Swelling/Death are Triggered by Short-Lived and Prolonged Light Stimulation of BV-1-Loaded Neurons. Pore formation on the neuronal surface is expected to impact the ion permeability of the membrane with an effect on the osmotic equilibrium of the cell. We therefore investigated the light-dependent changes in intracellular Ca^{2+} and Na^+ concentrations in BV-1-treated primary neurons loaded with either the fluorescent Ca^{2+} tracer Biotracker 609 Red Ca^{2+}-AM or the Na^+ tracer Ion NaTRIUM Green-2 AM. Neurons were incubated with a low concentration of BV-1 (100 nM) and stimulated with a single 3-s light pulse (see Figure S4) in the presence of synaptic blockers and TTX to prevent voltage-dependent Na^+ and secondary Ca^{2+} currents associated with AP firing (Figure 7A,C). While no detectable increase in intracellular Ca^{2+} levels could be observed in response to light stimulation both immediately after light offset and 30 s later (Figure 7B), Na^+ levels increased significantly both immediately after light offset and 30 s later (Figure 7D). These results further support the main role of Na^+ influx in mediating the effects of photostimulation and indicate a predominant

https://doi.org/10.1021/acsnano.4c01672
ACS Nano XXXX, XXX, XXX−XXX

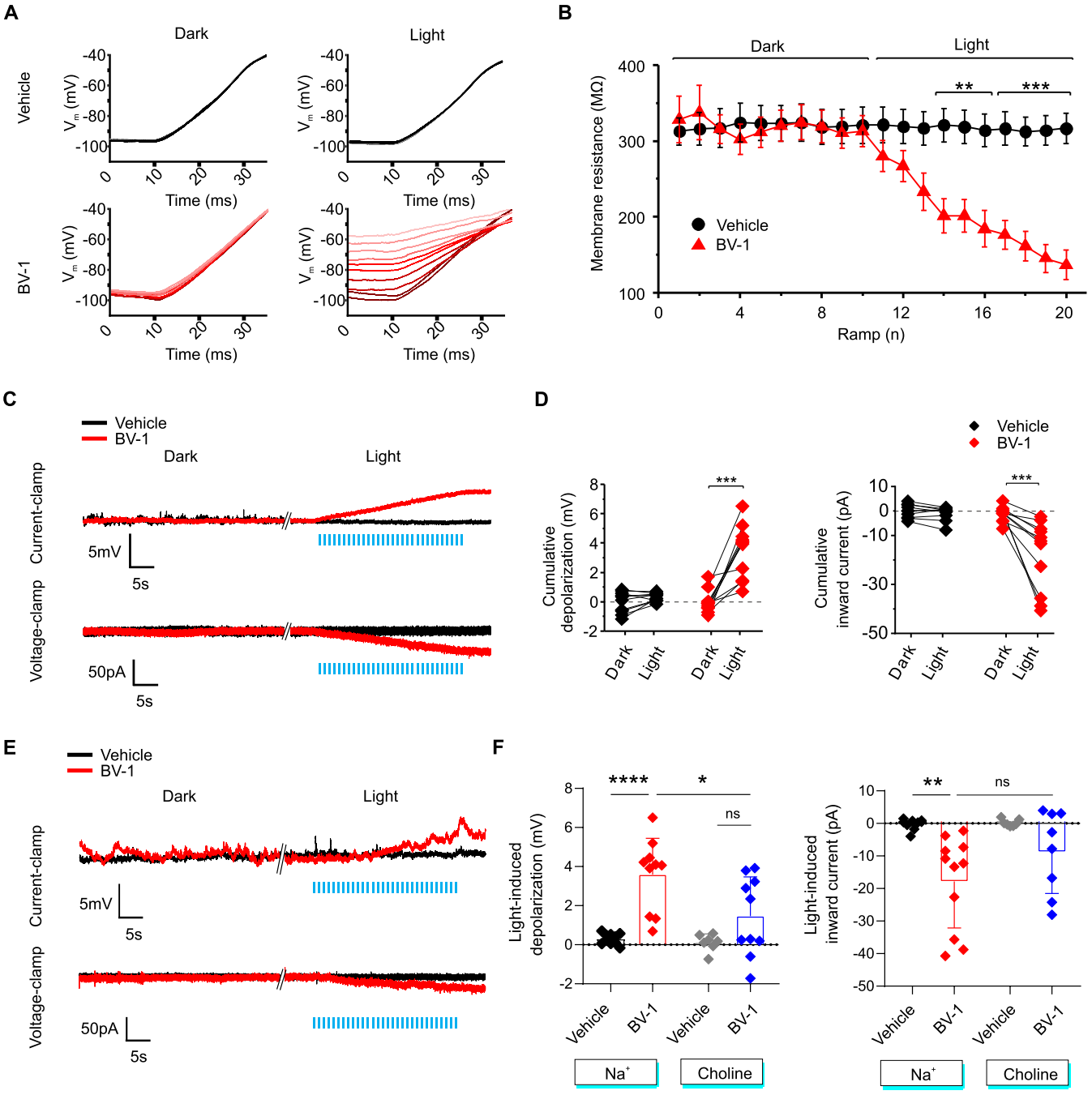

Figure 5. Light-dependent modulation of passive electrophysiological properties by BV-1. (A) Membrane voltage traces recorded with 10 CC ramps applied at 2 Hz, driving the membrane voltage from −95 to −40 mV in 20 ms in the dark and upon light stimulation (200 ms, 3 mW/mm^2) from neurons incubated with either vehicle or BV-1. (B) Membrane resistance calculated from the slope of the recorded voltage traces during 10 ramps in the dark and 10 ramps under light stimulation (n = 7 and 8 for vehicle and BV-1, respectively). (C) Representative membrane voltage traces recorded in CC configuration by holding the membrane voltage of primary hippocampal neurons at −70 mV (upper traces). Corresponding current traces recorded in the voltage-clamp (VC) configuration by clamping the voltage at −70 mV (lower traces). Cells were incubated with either vehicle (H_2O, black traces) or BV-1 (1 μM, red traces), and measurements were performed either in the dark or under light train stimulation (1 Hz, 20 ms, 30 light pulses, 3 mW/mm^2) in the presence of synaptic blockers and TTX (1 μM). (D) Cumulative membrane depolarization (left) and inward current intensity (I; right) modulation calculated at the end of the 40 s recorded sweeps (n = 10 and 11 for vehicle and BV-1, respectively). (E) Na^+ in the external medium was replaced with choline (135 mM). Representative membrane voltage traces recorded in CC configuration by holding the membrane voltage at −70 mV (upper traces), and corresponding current traces recorded in the voltage-clamp (VC) configuration by clamping the voltage at −70 mV (lower traces). Cells were incubated with either vehicle (black traces) or BV-1 (1 μM; red traces), and measurements were performed either in the dark or under light pulse stimulation (1 Hz, 20 ms, 30 light pulses, 3 mW/mm^2) in the presence of synaptic blockers and TTX (1 μM) in the extracellular medium. (F) Comparison of the cumulative light-induced depolarization (left) and inward current (right) in the presence of either Na^+ or choline in the extracellular medium (n = 10, 11, 7, 9 for vehicle/Na^+, BV-1/Na^+, vehicle/choline, and BV-1/choline, respectively). Statistics: *p < 0.05, **p < 0.01, ***p < 0.001; two-way ANOVA/Šídák's tests (B, F); Wilcoxon's test (D).

https://doi.org/10.1021/acsnano.4c01672
ACS Nano XXXX, XXX, XXX−XXX

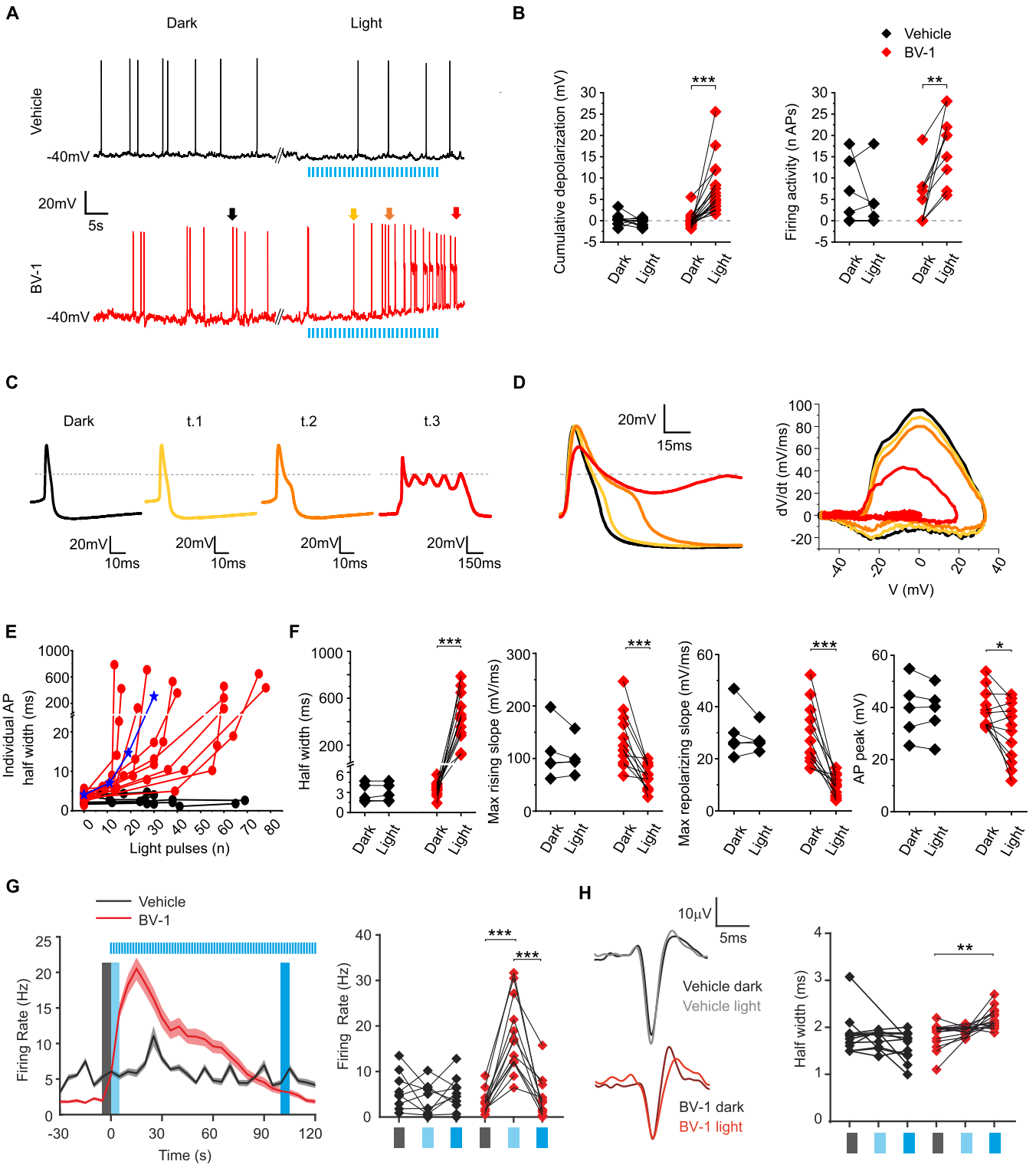

Figure 6. BV-1 light-dependent modulation of neuronal firing. (A) Action potential (AP) traces measured from neurons incubated with either vehicle (H_2O) or BV-1 (1 μM) in the dark or under light pulse stimulation (1 Hz, 20 ms, 30 light pulses, 3 mW/mm^2). Excitatory and inhibitory synaptic activities were pharmacologically blocked, and APs were recorded in CC configuration holding the membrane voltage at −40 mV. (B) Left: Cumulative depolarization (membrane voltage at 300 ms before the end of the 40-s protocol compared to the initial membrane voltage) in neurons incubated with either vehicle (black) or BV-1 (red) in the dark or under light pulse stimulation as described in panel A (n = 10 and 18 for vehicle and BV-1, respectively). Right: Firing activity calculated as the number of APs during 40 s in the dark and under light stimulation (n = 8 and 9 for vehicle and BV-1, respectively). (C) Zoom-in of the APs recorded in panel A (colored arrows) in the dark and at subsequent time points (black: dark; light yellow, orange, and red: refer to t.1, t.2, and t.3, respectively). (D) Superimposition of the four representative AP traces (left) and respective phase-plane plots (right). (E) AP half-width versus number of light pulses in individual neurons incubated with either vehicle (black) or BV-1 (red). Data from the representative recordings of panels A and C are shown in blue. (F) Phase-plane plot analysis of the AP waveform. From left to right: half-width, maximal rising slope, maximal

https://doi.org/10.1021/acsnano.4c01672
ACS Nano XXXX, XXX, XXX−XXX

Figure 6. continued

repolarizing slope, and AP peak recorded from either vehicle (black) or BV-1 (red)-treated neurons in the dark and at the end of the light stimulation (t.3) (n = 5 and 12 for vehicle and BV-1, respectively). Statistics: *p < 0.05, **p < 0.01, ***p < 0.001; paired Student's t-test/Wilcoxon's test. (G) BV-1 enhances the firing activity of primary neuronal networks on MEAs. Left: Mean firing activity of primary neurons incubated with either vehicle (black) or BV-1 (red) upon pulsed light illumination stated at time t = 0 s. Traces depict the average firing rate of a whole cell culture. Right: Ratio between the average firing rate in a 5-s window after stimulation and the basal average firing rate during the 5 s before stimulation. (H) Left: Representative waveforms of extracellularly recorded action potentials in neurons incubated with either BV-1 (red) or vehicle (black) upon pulsed light illumination. Right: Action potential half-width in neurons loaded with BV-1 either in the dark (black; t = −5 to 0 s) or during early (light blue; t = 0−5 s) and late (dark blue; t = 100−105 s) phases of pulsed illumination.

monovalent cation specificity of the pores generated by BV-1 upon light stimulation.

The demonstration of the opening of membrane pores by BV-1 under illumination led us to investigate neuronal viability and osmotic effects as a function of the duration of light stimulation. Primary neurons live labeled with Calcein Red/Orange were treated with BV-1 and subjected to continuous light stimulation at 3 mW/mm^2 for 1 s and imaged to measure the somatic area.

We observed that the light-induced inward ionic flux caused a progressive osmotic swelling of the neuronal cell body (Figure S8). Given the observed swelling and the substantial irreversibility of BV-1 effects, we investigated whether BV-1 could induce light-triggered neuronal death after prolonged continuous illumination (Figure 7E). BV-1 in the dark did not affect neuronal viability with respect to untreated or vehicle-treated neurons (Figure 7F, top). However, while neuronal viability was not affected upon short light stimulation (e.g., 10 light pulses of 200 ms at 1 Hz), a prolonged continuous illumination for 30 s induced significant cell death of ∼50%, as revealed by propidium iodide incorporation (Figure 7F, bottom).

BV-1 Elicits Similar Effects on the Passive Membrane Properties of Nonexcitable Cells. The data reported above demonstrate that BV-1 targets the phospholipid bilayer of neuronal cells and elicits complex light-evoked effects on the passive and active properties of these excitable cells. Before proceeding to test the effects of BV-1 in more complex neuronal networks, we wanted to verify whether the effects of BV-1 on the passive properties of the plasma membrane are exerted also in nonexcitable cells. To this aim, we chose HEK293 cells as a model system and subjected them to the same physiological protocols used for neurons (Figure 8). Also, HEK293 cells loaded with BV-1 incorporated the probe in the plasma membrane, as shown by precise colocalization with the plasma membrane marker CellMask (Figure 8A). The presence of BV-1 within the plasma membrane progressively decayed over time in culture to the same extent as observed in neuronal cells (see Figure 1D,E) due to membrane turnover (Figure 8B). When subjected to 30 s light train stimulation (20 ms light pulses at 1 Hz), BV-1-loaded HEK293 cells displayed a significant and progressive depolarization of the membrane potential during the light train that proceeded further after the end of the light stimulation interval (Figure 8C,D). We next investigated the changes in membrane resistance evoked by a series of light pulse stimulations (200 ms, 3 mW/mm^2, 1 Hz) by measuring the depolarization slopes induced by inward current ramps (Figure 8E).

As observed in neurons, the membrane resistance of BV-1-treated HEK293 cells, unchanged in the dark, displayed a significant and progressive decrease upon successive cycles of light stimulation, consistent with the light-triggered generation of membrane pores (Figure 8F).

Local Application of BV-1 Enables Light-Modulated Perforated Patch-Clamp Recordings. As BV-1 leads to cell swelling and death over prolonged light stimulation by irreversible membrane breaching, we sought to exploit these properties to induce local membrane optoporation in restricted patches of the membrane. Thus, we loaded the compound in the patch pipet containing the internal solution and obtained a cell-attached configuration (Figure 9A). The increase in the transient capacitive current, resulting from a 5 mV depolarizing step lasting 20 ms from a holding potential of −70 mV, was analyzed to determine the appearance of pores in the membrane patch upon prolonged pulsed light stimulation. More specifically, pore formation was defined when the Q_{peak} reached a plateau (Figure 9B). At the plateau, a significant increase in Q_{peak} and a significant decrease in patch resistance compared to the dark condition was observed, compatible with light-triggered membrane perforation (Figure 9C,D). A sample current-clamp recording of membrane voltage traces and AP triggering in a light-induced BV-1 perforated patch is shown in Figure S9. Interestingly, the observed average time required to initiate membrane poration and the time to reach the plateau were between 2 and 5 min (Figure 9E), which makes it consistently faster compared to existing perforating techniques using antibiotics such as amphotericin B, nystatin, or gramicidin.[39−41]

Light-Dependent Neuronal Firing and Activity Silencing by BV-1 in Blind Retinal Explants and Mouse Visual Cortex after Short and Prolonged Light Stimuli. The *in vitro* findings indicate that BV-1 is a *Janus* molecule that, inactive in the dark, can induce neuronal photostimulation or trigger neuronal death depending on the timing and intensity of the light stimulation. Thus, we investigated the light-dependent bifunctional properties of BV-1 in intact nervous tissue *ex vivo* in retinal explants and *in vivo* in the primary visual cortex (V1).

We explanted degenerate retinas from 12-month-old homozygous rd10 mice, a model of human retinitis pigmentosa, bearing a spontaneous mutation in the *PDE6* gene that promotes photoreceptor death but spares the inner retinal.[42,43] At this age, the retinas of homozygous rd10 mice are totally light insensitive, except for the small percentage of intrinsically photosensitive retinal ganglion cells (ipRGCs) expressing melanopsin.[44,45] Acutely explanted rd10 retinas incubated with either vehicle or BV-1 were placed onto MEAs in epiretinal configuration to record the firing activity of RGCs and stimulated with cyan light pulses (200 ms, 1 Hz) at increasing power density (0.5, 1, and 3 mW/mm^2). Although retinas were devoid of photoreceptors, an initial and short-lived increase in the light-evoked firing activity by ipRGCs was observed in both vehicle-treated and BV-1-treated retinas

https://doi.org/10.1021/acsnano.4c01672
ACS Nano XXXX, XXX, XXX−XXX

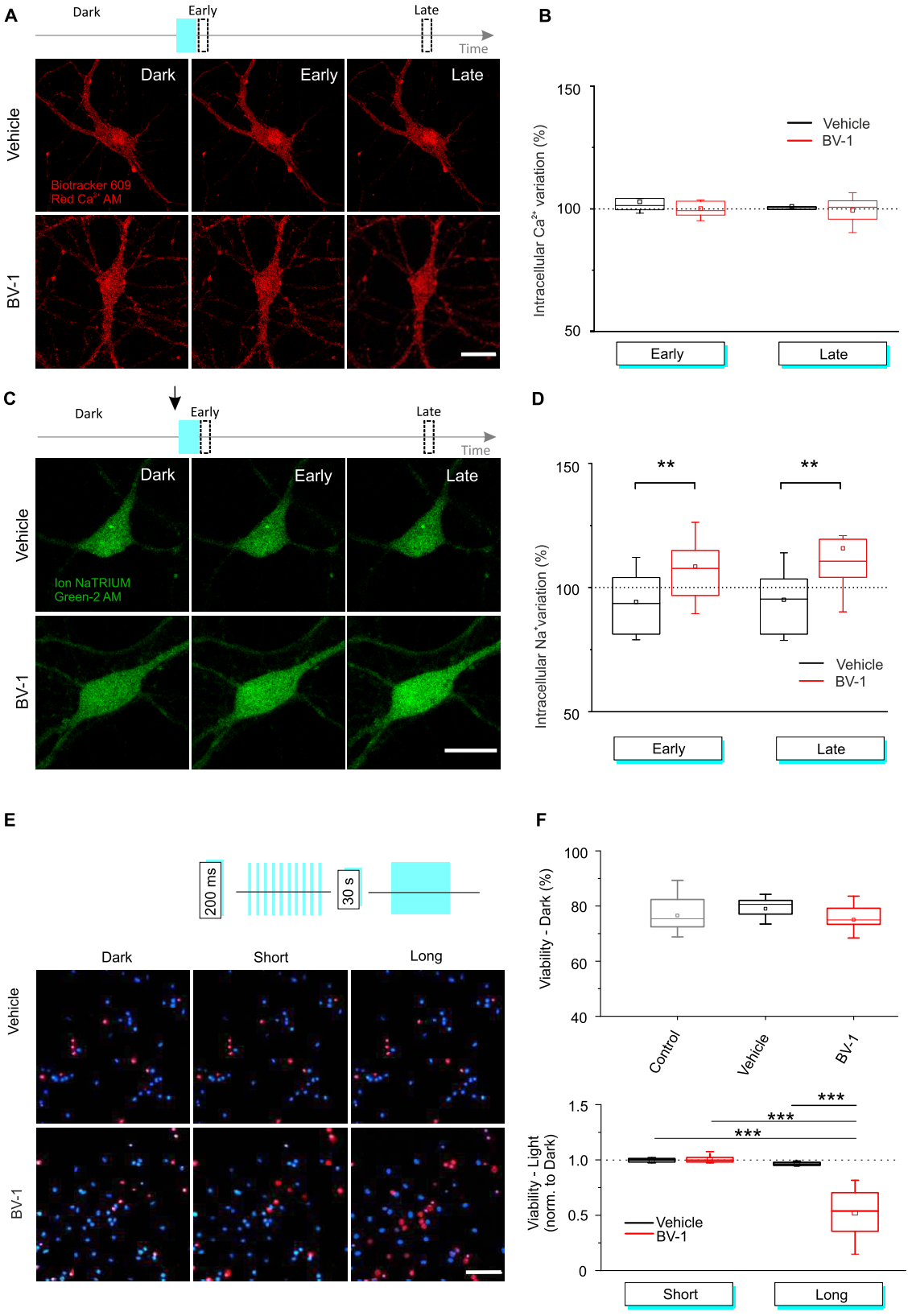

Figure 7. Light stimulation of BV-1-loaded neurons induces selective membrane permeabilization and cell death upon prolonged illumination. (A) Representative confocal images of intracellular Ca^{2+} levels using a Ca^{2+} fluorescent tracer (Biotracker 609 Red Ca^{2+} AM) at 0 and 30 s after light stimulation. Primary hippocampal neurons were incubated with either vehicle (H_2O, 0.1%) or BV-1 (100 nM). Ca^{2+} levels were acquired immediately after (Early) and 30 s after (Late) a single-pulse light stimulation (3 s at 3 mW/mm^2). All acquisitions were performed in the presence of synaptic blockers and TTX (1 μM) in the extracellular medium. Scale bar, 20 μm. (B) Quantification of the early and late changes in intracellular Ca^{2+} levels. The fluorescence increases of the Ca^{2+} tracer upon light stimulation were normalized by the fluorescence levels in the dark ($F/F_0 \times 100$) (n = 5 and 11 for vehicle and BV-1, respectively). (C) Representative confocal images of

https://doi.org/10.1021/acsnano.4c01672
ACS Nano XXXX, XXX, XXX−XXX

Figure 7. continued

intracellular Na^+ levels using a Na^+ fluorescent tracer (Ion NaTRIUM Green-2 AM) at 0 and 30 s after light stimulation. Basal levels of Na^+ were defined in the dark prior to incubation. After incubation with either vehicle (H_2O, 0.1%) or BV-1 (100 nM), neurons were light stimulated with cyan light at 3 mW/mm^2 for 3 s. Na^+ levels were acquired immediately after (Early) and 30 s after (Late) a single-pulse light stimulation (3 s at 3 mW/mm^2). All acquisitions were performed in the presence of synaptic blockers and TTX (1 μM) in the extracellular medium. Scale bar, 20 μm. (D) Quantification of the early and late changes in intracellular Na^+ levels. The fluorescence increases of the Na^+ tracer upon light stimulation were normalized by the fluorescence levels in the dark ($F/F_0 \times 100$) (n = 11 and 16 for vehicle and BV-1, respectively). (E) Neuron viability in the dark and upon sustained light stimulation. Neurons were incubated with either vehicle (H_2O; 0.1%) or BV-1 (1 μM), and viability was quantified in the dark, after a train of 10 short light pulses (200 ms, 1 Hz, 3 mW/mm^2) and after 30-s continuous light stimulus (3 mW/mm^2). Untreated primary neurons were used as controls. Neurons were stained with propidium iodide (PI; 1 μM; red) for dead cell counts and the nuclear stain Hoechst 33342 (1 μM, light blue) for total cell counts. Scale bar, 200 μm. (F) Quantification of cell viability in the dark (top) and after light stimulation (bottom). Percent viability in the dark (upper panel; n = 27, 21, and 56 fields for control, vehicle, and BV-1, respectively, from at least 3 independent preparations) and after the two light stimulation protocols (lower panel; n = 6 and 8 fields for control and BV-1, respectively, from at least 3 independent preparations). The viability data after light stimulation were normalized by the respective values obtained in the dark. Statistics: $^{**}p < 0.01$, $^{***}p < 0.001$; unpaired Student's t-test/Mann–Whitney's U-test (B, D); one-way ANOVA/Šídák's tests (F).

(Figure 10A). Besides this endogenous response to cyan light, BV-1-treated retinas responded to the train light stimulation with a significantly higher firing rate than the vehicle-treated ones.

To quantify this effect, we calculated the spike count difference between the 120 and 200 s window after light onset and during the same time interval in the darkness. The analysis confirmed that, in the early phase of light stimulation, BV-1-treated retinas responded to light with a 2-fold higher and more sustained firing activity than that displayed by vehicle-treated retinas (Figure 10B, left panel). However, in a later phase of the illumination protocol (between 320 and 400 s after light onset), the effect of BV-1 turned to a marked silencing of the RGC firing activity, while vehicle-treated retinas maintained a stable firing rate over time. Notably, the decrease in RGC firing progressed over time under light stimulation up to 300 s of the light train, leaving an ∼38% of the electrodes with a firing rate still not affected by illumination (Figure 10B, right panel).

To investigate the dual effect of BV-1 in the light-dependent modulation of neural activity *in vivo*, either BV-1 (500 μM in 1 μL of phosphate buffered saline, PBS) or PBS was stereotaxically injected in the V1 cortex of naïve mice that were subsequently implanted with an optical fiber for photostimulation and extracellularly recorded. When unfixed brain slices corresponding to the site of injection were examined for intrinsic BV-1 fluorescence, the area of diffusion of the molecule within cortical tissue was ∼200 μm in diameter around the site of the injection (Figure 10C). Optical stimulation was performed with 200 ms pulses at 1 Hz using a 430 nm LED at 40 mW/mm^2 power density. The stimulation protocol evoked a significant increase in the multiunit activity of V1 cortical neurons that was apparent toward the end of the light stimulation protocol (Figure 10D, left panel). When we calculated the ratio between the maximum firing rate measured after and before each protocol, a significant 2-fold increase in cortical firing activity was observed in BV-1 injected mice compared to vehicle-injected controls (Figure 10D, right panel). After the short-pulse light stimulation protocol, the injected mice were subjected to prolonged light stimulation for 30 s. Under these conditions, the retrospective immunohistochemical analysis of the injected areas revealed a significant increase in active caspase-3-positive neurons, testifying to the presence of light-triggered programmed cell death (Figure 10E).

DISCUSSION

Several types of organic molecular motors have been engineered to alter the membrane integrity, drilling holes, or forming ion-permeable pores in the membrane. Indeed, the membrane poration induced by these actuators emulates the activity of endogenous membrane permeabilization mechanisms activated by cell stressors, resulting in programmed cell death through plasma membrane breaching by protein/protein, protein/lipid, or lipid pores.[21] The biological applications of these synthetic actuators range from cancer therapy, antimicrobial drugs, and intracellular drug delivery to controlled membrane permeabilization.[46,47] The creation of hybrid interfaces between light-sensitive amphiphilic actuators and the neuronal membrane allows the trigger of light-dependent changes in the membrane passive properties that profoundly affect membrane potential and resistance, intrinsic excitability up to neuronal viability. Molecular motors and photoswitches that can operate nanomechanical actions on the membrane in response to optical stimuli have been engineered. Light-driven photoswitchable actuators can activate/deactivate ion channels or induce physical modification in the membrane that affects its passive properties.[18,19,48,49] Dual-component nanomotors, formed by a stator for membrane insertion and a rotor, drill holes in the membrane when activated by UV light with the purpose of selectively inducing "on-demand" cell death.[22,23]

In search of effective light-dependent actuators for these effects, we synthesized and characterized the amphiphilic compound BV-1. BV-1 spontaneously partitions into the membrane, is totally inert in the dark, and upon visible light illumination, transfers electronic density from the hydrophobic terthiophene fragment buried in the membrane core to the hydrophilic pyridinium ring, closely associated with the negatively charged membrane boundary. We found that the photopromoted chemical evolution of the BV-1 within a hydrophobic environment causes oxidation of membrane phospholipids by virtue of the terthiophene fragments that are known singlet oxygen sensitizers.[32,50] This result is in agreement with the photosensitizer effects recently observed in bacteria.[33] Interestingly, membrane poration predicted by MD simulations in the presence of oxidized phospholipids is greatly enhanced by the presence of photoactivated BV-1, likely due to the light-dependent BV-1 charge reorganization, which also induces its clustering. Moreover, inhibition of phospholipid oxidation by sodium azide pretreatment of primary neurons

https://doi.org/10.1021/acsnano.4c01672
ACS Nano XXXX, XXX, XXX−XXX

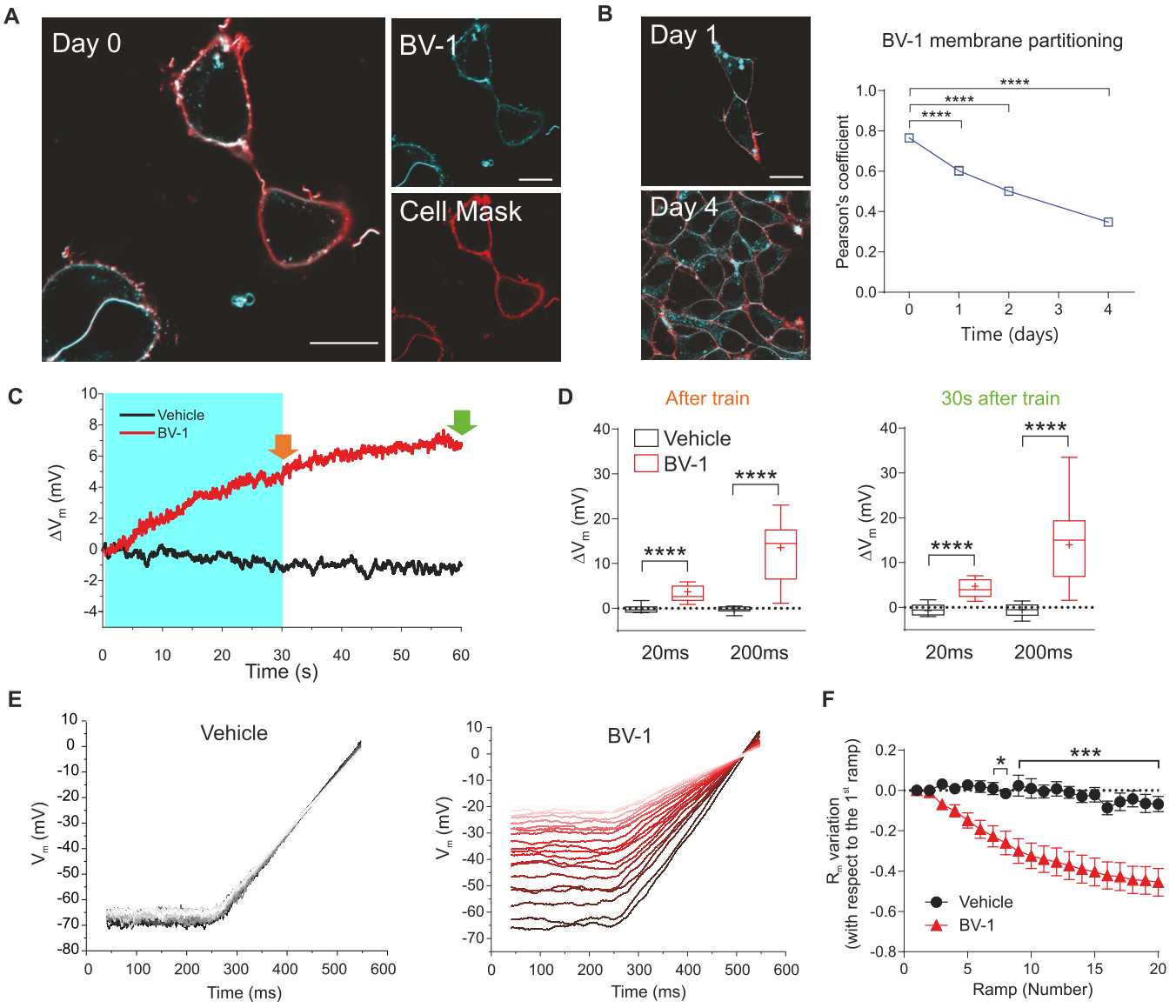

Figure 8. BV-1 partitions in HEK293 cell membranes and exerts light-evoked membrane depolarization. (A) Representative live confocal images of HEK293 cells loaded with BV-1 (1 μM, cyan) and CellMask membrane staining (5 μM, red). Scale bar: 20 μm. (B) The colocalization of BV-1 with the membrane was studied at various time intervals (0, 1, 2, and 4 days) after a single incubation with BV-1. Left: Representative images taken at days 1 and 4 after BV-1 loading (scale bar, 20 μm). Right: Pearson's overlap coefficient of BV-1 fraction colocalizing with CellMask shows a decrease of BV-1 in the membrane as a function of time (n = 22, 29, 22, and 24 fields for day 0, day 1, day 2, and day 4, respectively). (C) Representative traces recorded in the current-clamp configuration of HEK293 cells loaded with either vehicle (H_2O, black) or BV-1 (1 μM, red) for 5 min. Cell membrane potential was recorded in the dark for 1 s during a light train stimulation (1 Hz, light pulse duration: 20 ms, 25 mW/mm^2) and for 30 s again in the dark. (D) Box plots representing membrane potential variation immediately after the light pulse train (left; orange arrow in panel C) and 30 s after the train (right; green arrow in panel C) for cells loaded with either vehicle (H_2O, black) or BV-1 (1 μM, red) for 5 min. Cells were subjected to either short-lasting (20 ms) or long-lasting (200 ms) light pulses (20 ms: n = 19 and 16; 200 ms: n = 17 and 15 for vehicle and BV-1, respectively). (E) Representative traces recorded from HEK293 cells incubated with either vehicle (left) or BV-1 (right) upon 20 current-clamp ramps applied at 0.33 Hz, injecting current from −120 to 40 pA in 300 ms upon light stimulation (200 ms, 25 mW/mm^2). (F) Mean (±SEM) variations in membrane resistance calculated from the slope of the recorded voltage traces with respect to the first ramp (n = 16 and 24 for vehicle and BV-1, respectively). Statistics: *p < 0.05, ***p < 0.001, ****p < 0.0001; two-way ANOVA/Šídák's tests (B, F); Wilcoxon's test (D).

virtually abolishes the progressive light-evoked depolarization consequent to pore formation. Thus, the overall effect of phospholipid oxidation and BV-1 clustering is a local decrease in surface tension and stability, eventually leading to uncontrolled membrane fluidity, membrane thinning, and local collapses in the form of pores. Such structures can be observed by HS-AFM and appear to be monovalent cation-selective. The pores markedly decrease membrane resistance and, because of the ensuing inward Na^+ diffusion, produce an irreversible stepwise depolarization of the neuronal membrane over trains of light stimulation followed by osmotic imbalance over long light stimuli.

Similar to BV-1, polyene antifungal antibiotics have an amphiphilic character that allows them to penetrate the bilayer with a depth corresponding to a single leaflet to form two types of progressing pores: nonaqueous and fully permeable aqueous

https://doi.org/10.1021/acsnano.4c01672
ACS Nano XXXX, XXX, XXX−XXX

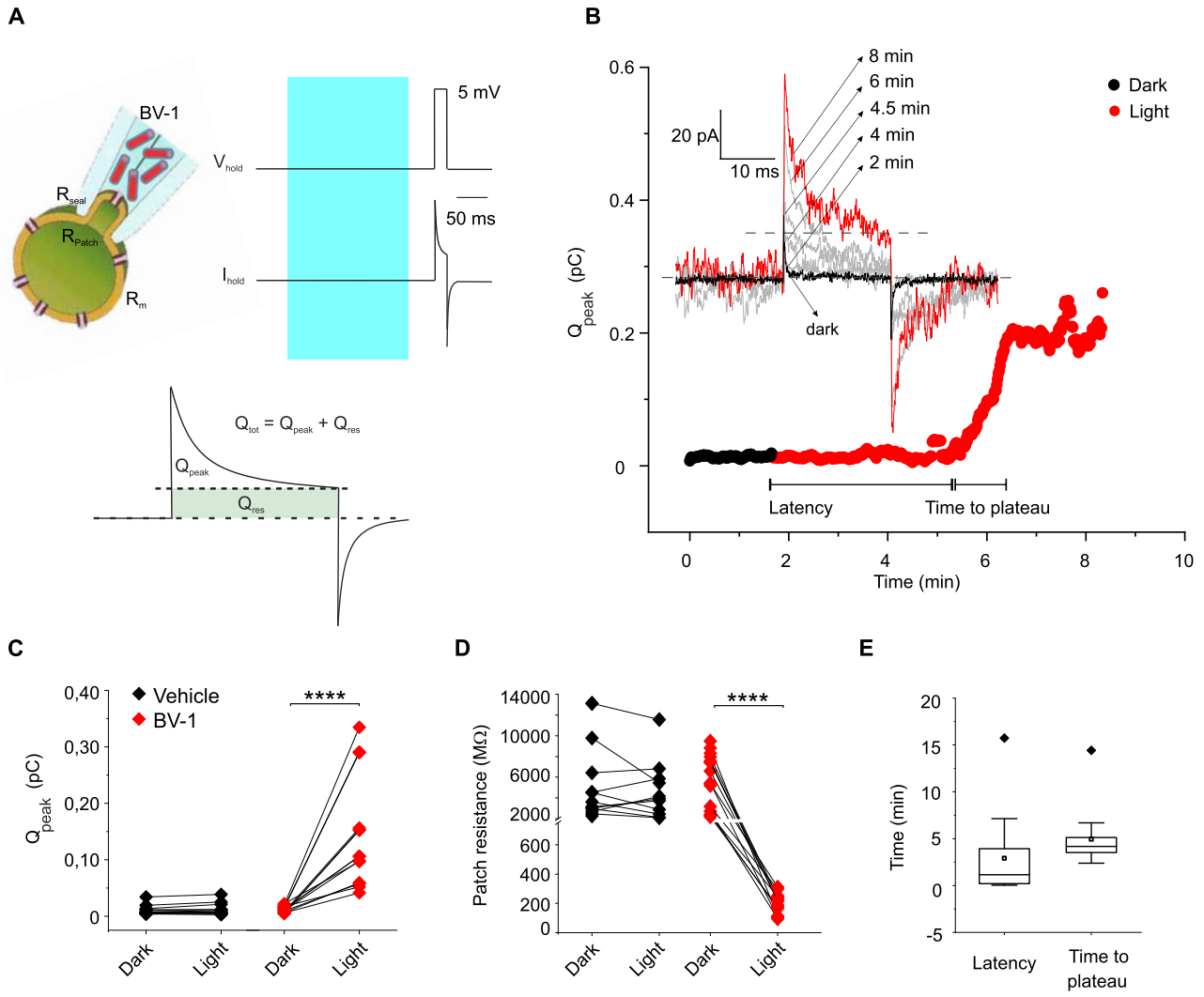

Figure 9. Light-triggered membrane poration dynamics from cell-attached to perforated patch configuration by BV-1. (A) Measurements were performed on primary hippocampal neurons in the cell-attached configuration with BV-1 (0.1 μM) in the patch pipet. The transient capacitive currents were elicited by a 20 ms depolarizing voltage step of 5 mV from a holding potential of −70 mV in the absence of light stimulation (Dark) or after successive cycles of illumination (200 ms, 3 mW/mm^2). (B) Representative charge modulation over time in the dark and upon illumination calculated as shown in the bottom part of panel A (Q_{peak}). The inset shows the capacitive currents in the dark (black trace) and at successive times during light stimulation (gray and red traces). (C, D) Q_{peak} amplitude (C) and patch resistance (D) in the dark and after subsequent cycles of illumination (left and right, respectively; n = 18 and 17 for vehicle and BV-1). (E) Distribution of the latency and time-to-plateau obtained by the evaluation of Q_{peak}/time relationships in BV-1-treated neurons (n = 17). Statistics: ***p < 0.001; paired Student's t-test/Mann−Whitney's U-test.

pores. Unable to span the membrane completely, nonaqueous pores can experience short-lived "open states", allowing the conductance of monovalent cations before evolving toward fully permeable aqueous pores.[51−53] Although the mechanism triggering the formation of pores by BV-1 depends on the light-dependent oxidation of membrane phospholipids, the BV-1-induced pores are reminiscent of the gramicidin or polyene pores but with the noticeable capacity of being regulated by light. Elements of similarity are the predicted membrane-embedded length of BV-1 of 2.1 nm (Figure S10), the association with membrane thinning and instability, and the gating properties with permeability to Na^+ but not to Ca^{2+}. Under these conditions, repetitive or prolonged light stimulation may promote maturation of the initial BV-1-induced pores into permanently open, fully permeable aqueous pores that eventually cause osmotic imbalance and cell swelling.

The physiological impact of BV-1 membrane incorporation in excitable cells, such as neurons, after mild light stimulation is an excitatory effect on neuronal activity. However, the progressive buildup of depolarization impairs the physiological voltage-dependent Na^+ and K^+ currents, causing a progressive widening of the AP in which, after repetitive light stimulation, the first spike is followed by a plateau populated by low-voltage *spikelets*, likely attributable to the decreased repolarizing K^+ currents and the progressive formation of BV-1 pore-like structures. While the response of primary neurons to short light pulses was stimulation of intrinsic excitability, the formation of BV-1 pore-like structures is proportional to the total irradiated energy, indicating that the massive depolarization in response to sustained illumination is a nonreversible process that induces osmotic imbalance, irreversible swelling and eventually death of the targeted cells.

https://doi.org/10.1021/acsnano.4c01672
ACS Nano XXXX, XXX, XXX−XXX

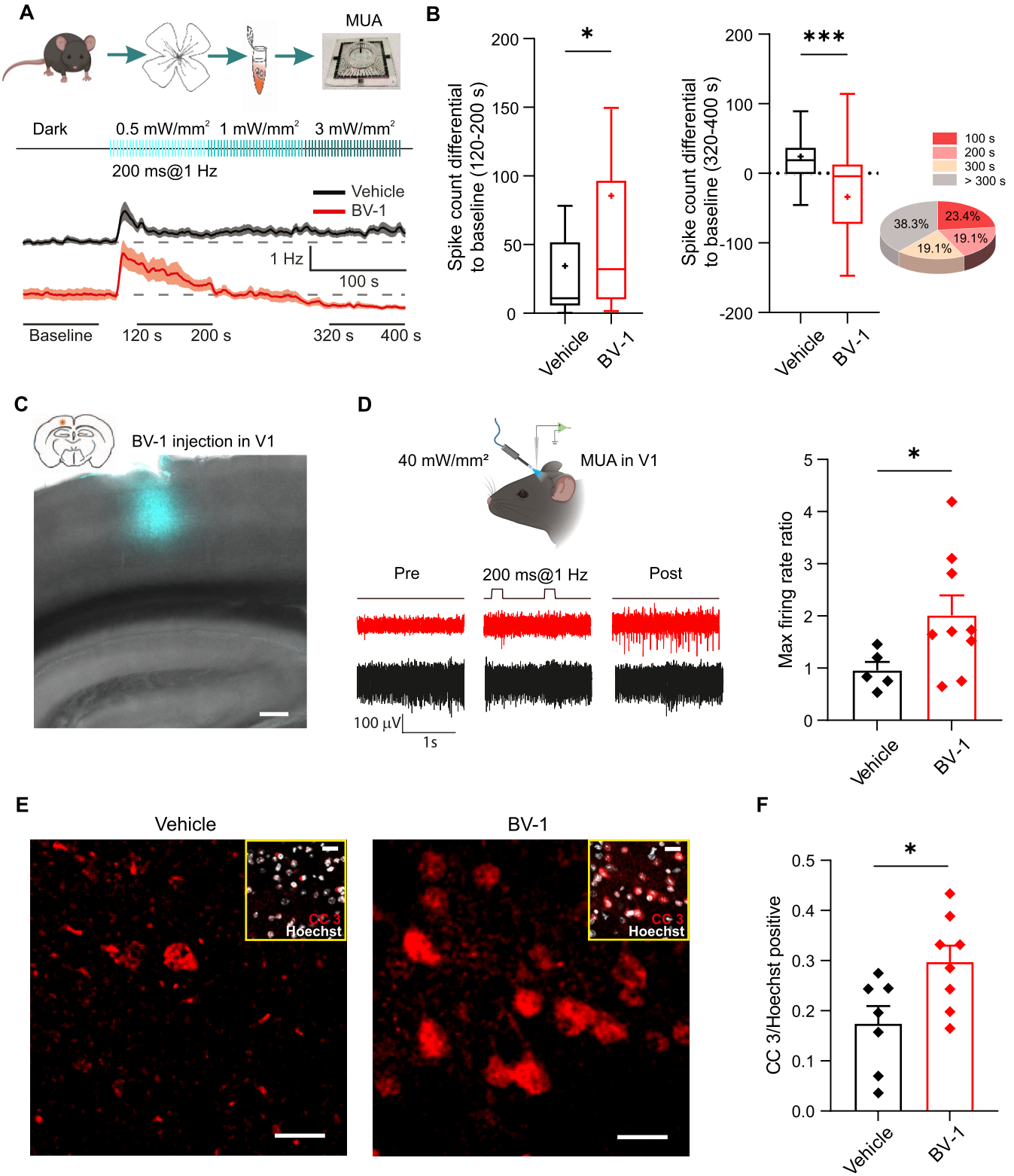

Figure 10. Light-dependent modulation of firing activity by BV-1 in blind retinal explants and primary visual cortex *in vivo*. (A) Schematic representation of the *ex vivo* experiments. Explanted blind rd10 retinas incubated with either vehicle (black trace) or BV-1 (red trace) for 30 min were positioned onto MEA in epiretinal configuration, stimulated with the illustrated illumination protocol (200 ms cyan light pulses, 1 Hz, 0.5, 1, and 3 mW/mm^2) to evoke RGC multiunit firing activity (MUA) represented as Peri-Stimulus Time Histograms (PSTHs). (B) Light-evoked RGC firing rates in blind retina explants. Left: Early changes in RGC firing. After an initial and short-lived physiological increase in the light-evoked firing activity (see panel A) ascribed to intrinsically photosensitive RGCs (ipRGCs), BV-1-treated retinas showed a significantly higher firing rate with respect to the vehicle-treated group. The effect was quantified as the spike count difference between the 120 and 200 s window after light onset and darkness (n = 43 and 38 electrodes for vehicle and BV-1, respectively, from 5 rd10 mice). Right: Late changes in RGC firing. Quantification of the firing rate in a later phase of the illumination protocol (between 320 and 400 s after light onset) revealed a significant decrease in the activity with respect to the spike count in the dark. The inset shows the percentage

https://doi.org/10.1021/acsnano.4c01672
ACS Nano XXXX, XXX, XXX−XXX

Figure 10. continued

of electrodes having a decreased firing at 100, 200, and 300 s after light onset. In ∼38% of the electrodes at times >300 s, the firing rate was not affected by the illumination (n = 43 and 38 electrodes for vehicle and BV-1, respectively, from 5 animals). (C) BV-1 (500 μM in 1 μL of PBS) was injected in the V1 cortex of naïve C57BL/6 mice (top-left schematic). A representative confocal image of V1 slices showed a spread of BV-1 of ∼200 μm (cyan), as detected through the molecule's intrinsic fluorescence. Scale bar, 200 μm. (D) Left: Schematic representation of the setup for *in vivo* MUA recordings in either vehicle- or BV-1-injected visual cortices (V1) light stimulated with an optic fiber in the proximity of the injection site (430 nm LED, 40 mW/mm^2). Representative traces of extracellular signals recorded before (pre), during (200 ms pulses at 1 Hz; 100 sweeps), and after (post) illumination of C57BL/6 mice injected with either vehicle or BV-1. Right: Mean ± SEM ratio between the maximum firing rates recorded after and before each stimulation protocol showed a significant increase of cortical activity in BV-1 injected mice compared to sham-treated controls (n = 5 and 9 animals for vehicle and BV-1, respectively; at least 3 recordings for each animal). (E) Left: Following the illumination protocol described in D, the injected areas were subjected to a prolonged stimulation of about 30 to 60 s. Representative confocal images of brain slices stained for active caspase-3 (Cas3, red) and nuclei (Hoechst 33342, white) in a region adjacent to the injection site that was subjected to prolonged illumination in either vehicle or BV-1 injected animals. The inset shows the merged channels. Scale bar, 20 μm. Right: Quantification of the ratio between the number of active caspase-3 and Hoechst 33342 positive neurons shows a significant increase in programmed cell death in brains injected with BV-1 with respect to the control group subjected to the same sustained light stimulation (n = 7 and 8 mice for vehicle and BV-1, respectively). Statistics: *p < 0.05, ***p < 0.001; unpaired Mann−Whitney's U-test.

As BV-1 leads to irreversible membrane breaching over prolonged light stimulation when applied to the whole cell, we exploited its biophysical properties to induce membrane optoporation in restricted patches of the neuronal membrane, making possible a light-triggered perforated patch-clamp configuration. Typically, standard whole-cell access to the neuron's interior causes a rapid washout of cytosolic components. One common use of gramicidin and antifungal polyenes is to open holes in the membrane patch of a patch-clamp pipet, yielding the perforated patch configuration that provides electrical access to the cell interior while avoiding dialysis of the cytoplasm by the pipet internal medium.[39−41,54] However, a major challenge of perforated patch experiments is that the perforating agent may disrupt the membrane seal and take several minutes to permeabilize the membrane patch. Here, we provide a proof-of-concept of a light-triggered perforated patch by localized application of BV-1 in the internal solution of the pipet. The resulting configuration resembles the standard perforated patch technique using gramicidin or polyenes but exhibits clear advantages, namely, (i) a stable seal can be obtained in the absence of changes in membrane properties in the dark; (ii) BV-1 is water-soluble and does not require organic solvents to be added to the internal solution; (iii) BV-1 can actuate an "on-demand" permeabilization by phasic light stimulation; and (iv) the light-triggered formation of BV-1 pores is much faster than that of antibiotics.

The *Janus*-like behavior of BV-1 observed *in vitro* was also addressed *ex vivo* and *in vivo* in intact nervous tissue. In blind retinal explants from rd10 mice, treatment with BV-1 elicited a higher RGC firing in response to brief light stimuli. However, similarly to primary neurons, RGC firing markedly dropped upon prolonged illumination. Similar results were obtained after the *in vivo* administration of BV-1 in the primary visual cortex of naïve mice, with an increase of the multiunit firing activity in the BV-1 positive area in response to low-frequency light pulses, followed by induction of programmed cell death upon prolonged and continuous illumination due to osmotic imbalance. Although the poration effect has profound effects in excitable cells such as neurons, it also occurs with other types of nonexcitable cells, such as HEK293 cells, confirming that BV-1 targets any plasma membrane irrespective of the cell type. Indeed, bacterial walls can also be targeted by BV-1, suggesting a possible use of the compound in photodynamic treatments.[33] For the critical viability of complex excitable cells such as neurons, we demonstrate that BV-1 is totally harmless in the dark, increases intrinsic excitability in response to short light pulses of light, and can cause osmotic imbalance, cell swelling, and death in response to intense and sustained light stimulation.

As a light-regulated membrane-embedded nanomachine, BV-1 can be compared to other molecular motors/switches that produce nanomechanical actions on the plasma membrane triggered by adequate stimuli,[22,23] with the advantage of being fully innocuous to cells in the dark and rapidly activatable "on demand" by visible light. Compared to laser-assisted optoporation technologies,[24,25] BV-1 does not require high-power pulsed lasers that often hamper the coupling of the technique to standard neuroscience investigations. Although plasmonic optoporation[28−31] needs less laser power, BV-1 is a more flexible tool offering the possibility to appropriately tune the extent of membrane targeting and the intensity/duration of the light stimuli to achieve full control over pore formation. Moreover, the possibility of performing a light-driven "*on-demand*" switch from cell-attached to whole-cell perforated patch configuration makes BV-1 a potential breakthrough in the field of advanced patch-clamp recordings.

CONCLUSIONS

Here, we have characterized that BV-1, a light-sensitive thiophene-based photochromic compound that spontaneously incorporates into the membrane, is totally inactive in the dark and opens monovalent cation-specific pore-like structures in the membrane under the control of light. The formation of such pores induces an early neuronal excitation and, upon prolonged stimulation, triggers cell swelling and programmed cell death. The ability to control the formation of the BV-1 assembled membrane pore with light and their gating properties represent important targets for the translational use of BV-1 among other advanced and recently developed pore-forming molecules for controlled permeabilization of cells for drug delivery or biocide purposes.[23,55,56] While its local application inside the patch pipet achieves a light-dependent perforated configuration that is harmless to the cell and performs better than classical antibiotic-based configurations, targeting BV-1 to specific cell populations in the brain has a high potential for future applications as light-triggered suppressor of tumor cells or hyperexcitable neurons within an epileptic focus.

https://doi.org/10.1021/acsnano.4c01672
ACS Nano XXXX, XXX, XXX−XXX

METHODS

Synthesis of BV-1. The amphiphilic donor−acceptor molecule BV-1 is composed of a π-conjugated electron donor−acceptor pair consisting of a terthiophene and a pyridinium moiety, an alkyl chain possessing a noncovalent affinity to the lipophilic core of the membrane and a hydrophilic head consisting of a quaternary ammonium cation and a hydroxyl-terminated unit. It was synthesized as described in detail in the Supplementary Methods.

^{1}H NMR Analysis of Phospholipids. Ten milliliters of a 0.20 mL/mL solution of a DOPC/choline 1:1 (mol:mol) containing 50 mM of BV-1 was irradiated at 365 nm using a TLC wood lamp. The solution was placed 5 cm from the wood lamp. After irradiation, all volatiles were removed, and the solid residue was characterized by NMR spectroscopy (Avance 400 MHz, Bruker, Milano, Italy) in DMSO-d_6 as the solvent.

Fluorescence Recovery after Photobleaching (FRAP). For FRAP experiments, lipids were prepared by mixing POPC:DOPS:cholesterol:Texas Red-DHPE (39.6:9.9:49.5:1% mol:mol, POPC, DOPS and cholesterol from Avanti Polar Lipids, Alabaster, AL; Texas Red-DHP from Invitrogen, Waltham, MA) at a final concentration of 2.5 mg/mL in chloroform, dried with nitrogen, and then placed under vacuum overnight. The preparation was then rehydrated to a density of 2.5 mg/mL in water, heated to 65 °C, vortexed 5 times, sonicated in a bath for 30 min, and stored at −20 °C. For preparing lipid bilayers, the liposome samples described above were diluted 10× in PBS containing 5 mM $CaCl_2$/20 mM $MgCl_2$, sonicated in the bath for 30 min and with an immersed probe (25 cycles at 40% amplitude, 0.2 Hz, and 40% duty cycle). After centrifugation at 20,000g, the lipid:cholesterol supernatant was deposited in custom-built wells on O_2 plasma-treated FluoroDishes (Greiner Bio-One, ThermoFisher Scientific, Waltham, MA) and heated for 30 min at 55 °C taking care to keep the deposited sample moist continuously. Lipid bilayers underwent 20× washes in PBS/5 mM $CaCl_2$/20 mM $MgCl_2$ to remove nonadsorbed lipid residuals. FRAP experiments were carried out with a Leica SP8 confocal microscope (63× magnification 1.4 NA, pinhole 3 AU). A 561 nm laser was used to bleach Texas Red-DHPE in a 15 μm diameter spot for a total time of 38.7 s. Each bilayer sample underwent 3 spatially different bleach procedures over time, namely, in the absence of BV-1 (control), after 15 min incubation with BV-1 (50 μM) in the dark and after light stimulation of BV-1 (9 mW/mm^2; 150 s). Images taken at a 0.5 Hz frame rate were subjected to segmentation in two regions of interest (ROIs): one matching the bleached spot and a second one outside the spot used as a reference. The average fluorescence intensity of the bleached ROI before, during, and after photobleaching was normalized with respect to the average fluorescence intensity of the reference spot to correct for photofading. The changes in normalized fluorescence intensity of the bleached spot after photobleaching were fitted with the single exponential $F(t) = A(1 - e^{-t/\tau})$, and the time constant τ was used to derive the diffusion coefficient $D = 0.224 \times \frac{r^2}{\tau/2}$, where r is the radius of the bleached spot.[57] The mobile fraction MF, indicating the amount of recovery after photobleaching, was calculated as $MF = \frac{F_\infty - F_0}{F_1 - F_0}$, where F_∞ is the total fluorescence recovery at time ∞, F_0 is the fluorescence intensity just after photobleaching, and F_1 is the fluorescence intensity before photobleaching. Image analysis was performed using ImageJ and MATLAB (The MathWorks, Inc.).

Langmuir−Blodgett Experiments. A Langmuir−Blodgett (LB) KSV 5000 NIMA trough was employed to study the pressure−area isotherm characteristics of the phospholipid films.[37] The surface pressure sensor is a platinum Wilhelmy plate, which was washed with ethanol and Millipore water before each experiment. Ultrapure Millipore water (18.2 MΩ) was used as a subphase. Solutions in chloroform of 1:1 POPC/cholesterol and 1:1:0.02 POPC/cholesterol/BV-1 were spread on the subphase (20 μL) by using a Hamilton syringe. To ensure the evaporation of the solvent, the analysis started 10 min after the dropping of the solution (holding time). In all experiments, the temperature was controlled at 24.0 ± 0.2 °C by an external circulating water bath. Monolayers were then compressed and expanded at 4 mm/min controlled barrier speed. Experiments were performed in the dark and under light stimulation. In the latter case, the LB trough was illuminated after the holding time by means of two LED lamps (470 nm power = 100 mW) to ensure uniform light excitation conditions. After each analysis, the trough was washed with ethanol and Millipore water.

Atomic Force Microscopy (AFM). POPC and ovine cholesterol (chol) were purchased from Avanti Polar Lipids. Supported lipid bilayers (SLBs) were prepared according to previously described protocols.[58] Briefly, POPC and POPC/chol = 1:1 small unilamellar vesicles (SUVs) were prepared by first dissolving in chloroform and mixing the lipids at the indicated molar ratio. The solubilized lipids were then dried under a gentle nitrogen stream and left overnight under vacuum to remove any leftover traces of the solvent. Subsequently, the dried lipids were resuspended into standard AFM buffer (150 mM NaCl, 20 mM HEPES-NaOH at pH 7.4, and 2 mM $CaCl_2$) and sonicated (ultrasonic bath, 40 kHz) for 30 min to generate SUVs. Before HS-AFM imaging, 2 μL of diluted SUV suspension (0.1 mg/mL) was deposited onto a freshly cleaved mica disk to form SLBs through vesicle fusion. After 15 min incubation, excess lipids were removed by thorough rinsing with standard AFM buffer. All AFM observations were performed in the tapping mode using a laboratory-built apparatus as previously described.[59] Briefly, a glass sample stage (diameter, 2 mm; height, 2 mm) with a thin mica disc (2 mm in diameter and ∼0.1 mm thick) fixed on top with cyanoacrylate glue was attached onto the upper face of the z-scanner by a drop of nail polish. The sample stage with the SLB of choice adsorbed on top was immersed in a liquid cell filled with ∼100 μL standard AFM buffer. Short cantilevers (BL-AC10DS-A2, Olympus) with a nominal spring constant of ∼100 pN/nm, a resonance frequency of ∼0.5 MHz, and a quality factor of ∼1.5 in water were used (Marchesi et al., 2018). An amorphous carbon tip was fabricated on the original AFM tip by electron beam deposition (∼500 nm in length and apex tip radius of ∼4 nm) and etched under argon plasma (Tergeo, PIE Scientific LLC, Union City, CA) to further sharpen the apex radius. The cantilever free oscillation amplitude A_0 and set point amplitude A_s were set at ∼2 nm and around 0.9 × A_0, respectively. Under these conditions, the energy delivered by a tip−sample interaction is 1−3 kBT on average.[60] For sample irradiation, a blue LED diode (460 nm) was used. Light intensity and pulse width were manually controlled with an LED driver (LEDD 1B, ThorLabs, Newton, NJ) operated in constant current mode. The used LED power density after the objective lens was in the range of 11−12 mW/mm^2. All experiments were performed at room temperature (24−26 °C) and dark ambient conditions. Data were collected using laboratory-developed software based on Igor Pro 8 (WaveMetrics) and Visual Basic.NET (Microsoft).[61] HS-AFM movies were x,y-drift-corrected using the ImageJ plugins "*Template Matching and Slice Alignment*" (https://sites.google.com/site/qingzongtseng/template-matching-ij-plugin). Image flattening was achieved by means of plane or second-order polynomial surface fitting, as appropriate. Afterward, median (0 order) line-by-line leveling was used to remove height offsets along the fast scan axis.[62] These steps were performed using in-house software routines developed in MATLAB (MathWorks), available at https://github.com/arin83/U1067/.

For AFM breakthrough experiments, the formation of SUVs and deposition on mica surfaces were performed as previously described.[38] BV-1 was manipulated under minimal red light. After the addition of BV-1 to the sample, we waited 10 min before the measurements in the dark and a further 10 min after light stimulation. The Xenon light of the fluorescence microscope was used as the illumination source, using a GFP filter excitation at 470/40 nm. On each experimental day, the tip was not changed between the experiments. The breakthrough forces were recorded from 500 to 700 curves from each sample, obtained by acquiring at least five grids of 10 × 10 points in a 15 × 15 μm square. The breakthrough force, corresponding to a sudden penetration of the AFM tip through the membrane, i.e., a local maximum of the force jump on the force−distance curve, was analyzed using a Python code based on PyFMLab software.[63] The breakthrough force was determined by localizing the local maximum

https://doi.org/10.1021/acsnano.4c01672
ACS Nano XXXX, XXX, XXX−XXX

in the force−distance curve. After obtaining the breakthrough force from each curve, a histogram of the distribution of the breakthrough forces was obtained and fitted to a Gaussian distribution to obtain the mean and standard deviation.

Molecular Dynamics Simulations. All-atom MD simulations of BV-1 were performed in the presence of a model membrane bilayer of 1-palmitoyl-2-oleoyl-phosphatidylcholine (POPC) made of 112 lipid molecules (56 per leaflet) and water. We simulated separately the spontaneous insertion of a single BV-1 molecule in the membrane and eight molecules embedded in the membrane in a dark or light configuration. Starting coordinates for the systems were generated with the CHARMM-GUI web server,[64] using pre-equilibrated lipid structures. All simulations were run with NAMD v2.12 code[65] using the CHARMM36 force field[66] and the TIP3P model for water molecules. CHARMM-compatible topology and parameters for BV-1 were obtained using the CHARMM General Force Field (CGenFF)[67] and atomic charges from time-dependent density functional theory (TDDFT) calculations (see below). The total electrostatic charge of each system was neutralized by the addition of physiological concentrations of counterions. The time step for integrating the equations of motion was 2 fs, and covalent bonds to hydrogens were constrained using SHAKE.[68] Simulations were performed with periodic boundary conditions in the NPT ensemble, with P = 1 atm and T = 310 K, using a Langevin thermostat with a damping constant of 5 ps^{-1} and a Langevin piston with a constant decay of 100 ps^{-1} and an oscillation period of 200 fs. A flexible unit cell was used with a constant ratio in the x−y plane. Long-range electrostatic interactions were computed using the particle-mesh Ewald method, with a fourth-order spline and 1 Å grid spacing.[69] The following simulations were performed: five independent, 1 μs runs for spontaneous insertion in the membrane of a single dark BV-1 and two runs of 2 μs each with eight copies of BV-1 embedded in the membrane, in dark or light conformation. When multiple copies of BV-1 were considered, they were distributed symmetrically in the upper and lower leaflets.

For the simulations containing oxidized lipids, parameters and topologies from the recently updated CHARMM-GUI library were used.[70] We employed PoxnoPC (1-palmitoyl-2-(9′-oxo-nonanoyl)-*sn*-glycero-3-phosphocholine), a stable oxidation product of POPC bearing a carbonyl group at the end of the truncated sn-2 chain. Two systems comprising a membrane with 67% PoxnoPC and 33% POPC lipids were built, and 8 BV-1 molecules in light conformation were added to one of them, four per layer. The membranes were solvated with TIP3P water and counterions and simulated in the NPT ensemble (T = 310 K and P = 1 atm) using NAMD v2.12 and the CHARMM36 force field. All simulation parameters and algorithms were the same as those of the nonoxidized systems described above.

Density Functional Theory Calculations. The electronic and optical properties of BV-1 were investigated in the framework of time-dependent density functional theory (TDDFT) using the ORCA suite of programs.[71,72] A configuration of the solvated BV-1 was extracted from a preliminary MD trajectory, and it was fully optimized using a revised PBE0 hybrid functional with 37.5% of exact exchange,[73] suitable for accurately describing the strong charge-transfer transition which dominates the absorption spectrum of BV-1, and the D3BJ dispersion correction.[74] The Kohn−Sham orbitals have been expanded on a Gaussian-type def2-TZVPP basis set.[75] The corresponding def2/J basis was also used as an auxiliary basis set for Coulomb fitting in a resolution-of-identity/chain-of-spheres (RIJCOSX) framework. Time-dependent DFT calculations were performed using the same functional and the same basis sets; a large basis of 600 vectors connecting occupied and unoccupied Kohn−Sham orbitals was used for the calculations of the first 30 electronic transitions of the absorption spectrum of the molecule, shown as Gaussian convolution of electronic transitions (fwhm = 4000 cm^{-1}) in Figure S1. Solvent effects have been included in the calculations through the linear-response conductor-like polarizable continuum model (LR-CPCM).[76] Mulliken charges obtained in the case of the ground and the first singlet excited state using this setup were then employed to improve the accuracy of the force field in MD simulations, with the aim of introducing a realistic yet cost-effective differentiation between the ground and excited state in large systems.

Ethical Approval and Animal Handling. All animal manipulations and procedures were performed in accordance with the guidelines established by the European Community Council (Directive 2014/26/EU of 4 March 2014) and were approved by the Italian Ministry of Health (Authorization # 357/2019-PR). C57BL/6 and rd10 mice were bred under standard conditions with *ad libitum* access to food and water under a 12/12 h light/dark cycle.

Cultures of Primary Hippocampal Neurons. Primary hippocampal neurons were prepared from WT C57BL/6 J (Charles River, Calco, Italy) mice. Animals were anesthetized by CO_2 inhalation and sacrificed by cervical dislocation. Embryos at embryonic (E) day 17/18 were immediately removed by cesarean section. Hippocampi were dissected in iced cold media and incubated in 0.25% Trypsin-EDTA (Gibco ThermoFisher Scientific) at 37 °C for 15 min for enzymatic digestion. Cells were then mechanically dissociated with a fire-polished Pasteur pipet, and cell viability was determined by Trypan Blue exclusion assay. Neurons were plated onto poly-D-lysine (0.1 mg/mL, Sigma-Aldrich, Milano, Italy)-coated 18 mm glass coverslips (4 × 104 cells/coverslip) in the culture media containing Neurobasal media (Gibco) supplemented with 2% B27 (Gibco), 0.5 mM glutamate (Gibco), and 1% penicillin−streptomycin (Gibco) and kept at 37 °C in a 5% CO_2 humidified atmosphere. All experiments were performed at 14−18 days *in vitro* (DIV).

Light Stimulation Protocol. All light stimulations during electrophysiological recordings were performed using a Spectra X Light Engine LED system (Lumencor, Beaverton, OR) fiber-coupled to an upright Nikon FN1 microscope (Nikon Instruments, Tokyo, Japan). The light source emission was in the cyan spectrum (470 ± 10 nm) to match the BV-1 absorption spectrum. For the viability assay, neurons were stimulated using an Eclipse-80i upright epifluorescence microscope (Nikon Instruments). The light source emission was filtered through an Iridian single-band filter set optimized for fluorescein isothiocyanate (FITC) (470 nm). During live confocal imaging experiments, neurons were stimulated using a Hg fluorescence lamp (Leica Microsystems, Wetzlar, Germany). In all imaging setups, the power density used was 3 mW/mm^2, as measured at the output of the respective microscope objective.

Patch-Clamp Electrophysiology of Primary Neurons. Whole-cell patch-clamp recordings of low-density primary hippocampal neurons were performed in the dark at room temperature (22−24 °C) using an EPC10 (HEKA Elektronik, Reutlingen, Germany) amplifier. Borosilicate glass pipettes (Kimble, Kimax, Mexico) with a 3−4 MΩ resistance were used. For all experiments, if not differently stated, pipettes were filled with an intracellular solution containing (in mM): 126 K gluconate, 4 NaCl, 1 $MgSO_4$, 0.02 $CaCl_2$, 0.1 BAPTA, 15 glucose, 5 HEPES, 3 ATP, and 0.1 GTP (pH 7.3 with KOH). Cells were maintained in standard extracellular Tyrode solution containing (in mM) 140 NaCl, 2 $CaCl_2$, 1 $MgCl_2$, 4 KCl, 10 glucose, and 10 HEPES (pH 7.3 with NaOH). All chemicals were purchased from Sigma-Aldrich (St. Louis, MO), except for Tetrodotoxin (TTX) from Tocris Bioscience (Bristol, U.K.). Cells with leak currents >200 pA or series resistance (R_s) > 20 Ω were discarded. Hippocampal neurons were incubated with either vehicle (H_2O; 0.1/1%, v/v) or BV-1 (0.1/1 μM) for 5 min at room temperature and then washed twice with extracellular medium. Neurons were recorded acutely after incubation (day 0) or 4 days after (day 4).

Light-Induced Neuronal Activity Modulation. To study light-dependent membrane voltage modulation in neurons synaptically isolated from the neuronal network, D-AP5 (50 μM), CNQX (10 μM), and Bicuculline (30 μM) were added to the extracellular medium to block excitatory and inhibitory transmissions. Current-clamp recordings of light-induced depolarization were performed by holding the cell at its resting membrane potential (I_h = 0) and stimulating it with 7 subsequent 20 or 200 ms light pulses. The resulting depolarization was calculated in a 300 ms time window after each light pulse and compared to the basal membrane potential before stimulation. Modulation of membrane resistance was measured with current-clamp (CC) ramps driving the membrane voltage from −95

https://doi.org/10.1021/acsnano.4c01672
ACS Nano XXXX, XXX, XXX−XXX

to −40 mV in 20 ms to calculate the corresponding slope of the recorded voltage traces. The protocol was repeated for 10 cycles in the dark, followed by 10 cycles with light pulses (200 ms) preceding the CC-ramp. To study the features of APs, train stimulation was used with 20 ms light pulses at a frequency of 1 Hz. Current-clamp recordings of the firing activity were sampled at 50 kHz and low pass filtered at 10 kHz using an EPC10 amplifier (HEKA Elektronik), and the following parameters were measured: (i) half-width (ms), calculated at the membrane voltage of −20 mV and (ii) AP peak (mV) calculated as the most positive voltage reached during depolarization. The plot of the time derivative of voltage (dV/dt) vs voltage was then constructed (phase-plane plot) to extract (i) maximal rising slope (mV/ms) from the positive peak and (ii) maximal repolarizing slope (mV/ms) from the negative peak. Four representative time points were selected for each cell: one in the dark and three during the light stimulation protocol (t_1, t_2, and t_3). To inhibit lipid oxidation, sodium azide (NaN_3, Sigma-Aldrich) was directly added to primary hippocampal neurons at DIV 14 in a Neurobasal culture medium at 1 μg/mL. Cultures were incubated with either NaN_3 or fresh Neurobasal (control) for 1 h before the incubation of both experimental groups with BV-1 (1 μM) or vehicle for 5 min.

Study of Subthreshold Membrane Properties. To study the contribution of voltage-gated ion channels to light-induced depolarization, in addition to synaptic blockers, TTX (1 μM) was added to the extracellular medium to block voltage-gated Na^+ channels. Current- and voltage-clamp recordings were performed at a holding potential of −70 mV. Cells were stimulated with a 30-s train of light stimuli (1 Hz, 20 ms), and the membrane potential and inward current at the end of the 40-s trace were compared to the values at the beginning of the protocol, respectively. To evaluate the possible reversibility of the observed light-induced depolarization, neurons were incubated with either vehicle (H_2O, 0.1% v/v) or BV-1 (0.1 μM) and then stimulated with light pulses of increasing duration (20−3000 ms). The extent of depolarization was measured in two 300 ms time windows: the first starting at the light pulse offset (early depolarization) and the second at the end of the 8 s recording time (late depolarization). To study membrane permeabilization upon light stimulation, a standard internal solution was used in combination with an extracellular solution, where Na^+ was replaced by choline (135 mM), and current- and voltage-clamp recordings were performed at a holding potential of −70 mV, as previously described.

Light-Induced Modulation of Sodium and Potassium Conductances. In order to investigate the modulation of voltage-dependent sodium currents, the intracellular solution contained (in mM): 120 Cs methanesulfonate, 4 NaCl, 0.02 $CaCl_2$, 1 $MgSO_4$, 0.1 EGTA CsOH, 10 phosphocreatine, 3 ATP-Na_2, 0.1 GTP-Na, 10 HEPES (pH 7.3 with CsOH), and an external "blocking" solution containing (in mM): 120 NaCl, 3 KCl, 2 $CaCl_2$, 1 $MgCl_2$, 10 HEPES, 11 Glucose, 20 TEA-Cl, 1 4-aminopyridine, 0.5 $CdCl_2$. Membrane voltage was held at −40 mV, and voltage-dependent Na^+ currents were elicited through 5 mV voltage steps reaching 20 mV. The recorded traces were analyzed to obtain the voltage−current (I/V) curve and the time constant of current decay (corresponding to Na^+ channel inactivation) at −10 mV. Steady-state voltage-dependent K^+ currents were studied using standard intracellular and extracellular solutions, and I/V curves were obtained by depolarizing neurons for 200 ms with voltage steps from −20 to 60 mV applied in 10 mV increments from a holding potential of −40 mV. Data were analyzed using FitMaster v2 × 90.1 (HEKA Elektronik) together with Prism 6.07 (GraphPad) and OriginPro 9 (OriginLab) software.

Multielectrode Array Recordings on Primary Cortical Neurons. Primary cortical neurons were prepared as described above. Neurons were plated onto poly-D-lysine (0.1 mg/mL, Sigma-Aldrich)-coated 18 mm glass coverslips (50,000 cells/well) in the culture media containing Neurobasal media (Gibco) supplemented with 2% B27 (Gibco), 0.5 mM glutamate (Gibco), and 1% penicillin−streptomycin (Gibco) and kept at 37 °C in a 5% CO_2 humidified atmosphere. At DIV 14, 50% of the culture medium was replaced in each well, and the experiments were performed at 20−21 DIV. Each culture was incubated with either BV-1 (1 μM) or vehicle for 15 min. Light stimulation was delivered with a Lumos 48 (Axion Biosystems, Atlanta, GA) peaking at 475 nm, whose light spot covered the entire area of the wells (power density: 0.66 mW/mm^2). Signals were recorded at 12.5 kHz, and after a 30-s baseline period in the dark, both vehicle and BV-1 incubated cultures were stimulated with 120 pulses of cyan light at 1 Hz (duty cycle 20%; 120 s stimulation). Spike detection was performed on high-pass filtered data (cutoff frequency 200 Hz) using a customized script in MATLAB (R2023a, The MathWorks, Inc.) with a detection threshold set above 5-fold the standard deviation (SD) of the whole trace. Electrodes showing a mean firing frequency under 1 Hz were filtered out. Firing rate traces were obtained by binning spike counts in 5-s windows. The average firing rate was calculated in the 5-s bins immediately before, immediately after, and at 100−105 s after the onset of stimulation. To analyze the waveform of the extracellularly recorded APs, all firing events in the 3 time windows underwent subsequent analysis of their half-width. Each AP detected by a single electrode was averaged, and the resulting AP waveform was fit with a cubic spline to calculate half widths.

Cell Viability Assays. Primary hippocampal neurons were either incubated with the vehicle (H_2O, 0.1%) or with BV-1 (1 μM) for 5 min at room temperature. Cells were then stained with propidium iodide (PI; 1 μM) for cell death and with Hoechst 33342 (1 μM) for nuclei visualization for a further 5 min. Images were acquired at 10× (0.5 NA) magnification using an Eclipse-80i upright epifluorescence microscope (Nikon Instruments). Cell viability was obtained by the ratio of propidium iodide (PI)-/Hoechst 33342 positive cells. Cell viability was compared between neurons that were untreated, incubated with the vehicle, or incubated with BV-1. Neurons loaded with either BV-1 or vehicle were then subjected first to a train stimulation of 10 light pulses of 200 ms at 1 Hz and then to a continuous illumination for 30 s. PI was present in the extracellular medium all along the experiment, and cell viability was recalculated 5 min after each stimulation. Image analysis was performed using ImageJ software and the Cell Counter plugin.

Confocal Live Imaging. Primary hippocampal neurons were incubated with BV-1 (1 μM, 5 min) in culture media. To evaluate the distribution of BV-1, the neuronal surface was labeled with CellMask (5 μM, 5 min) and live imaging was performed with a SP8/HyD confocal scanning microscope equipped with super-resolution LAS-X Lightning deconvolution software (Leica Microsystems). Colocalization of the two fluorescence signals was analyzed using ImageJ plugin "JACoP". The observed swelling of neuronal soma upon light stimulation was quantified using CellTrace Calcein Red-Orange (2 μM; ThermoFisher Scientific) as an intracellular marker. Cells were first incubated for 5 min with either BV-1 (1 μM) or vehicle (H_2O; 0.1% v/v) and then with the fluorescent dye for 10 min at room temperature. The somatic area was first quantified in the dark and then 1 min after 1 s light stimulation. To study light-induced membrane permeabilization, neurons were first incubated with a Ca^{2+}-tracer (Biotracker 609 Red Ca^{2+}-AM, 3 μM) for 30 min at 37 °C and then with either vehicle (H_2O; 0.1% v/v) or BV-1 (0.1 μM) for 5 min. Calcium levels were acquired in the dark, immediately after a 3-s light pulse (t = 0 s) and 30 s later (t = 30 s). Sodium intracellular levels were monitored by incubating neurons with the Na^+ tracer (Ion NaTRIUM Green-2 AM (2 μM; Interchim Bioscience, Montluçon, France). Given the overlap between the absorption spectra of BV-1 (λ_{ex} 472 nm, λ_{em} 637 nm, see Figure 1A) and Ion NaTRIUM Green-2 AM (λ_{ex} 525, nm, λ_{em} 545 nm), either vehicle (H_2O; 0.1% v/v) or BV-1 (0.1 μM) was added after acquisitions in the dark to avoid interference with the Na^+ tracer excitation. After 5 min, neurons were stimulated with a 3-s light pulse and Na^+ levels were acquired in the dark, at the light offset (early), and 30 s later (late).

Studies in Non-Neuronal Cells. The immortalized cell line HEK293T (Human Embryonic Kidney) was provided by the American Type Culture Collection (ATCC, Manassas, Virginia). Cells were cultured in T-25 cell culture flasks containing Dulbecco's modified Eagle's medium high glucose (DMEM-HG) culture medium, supplemented with 10% heat-inactivated fetal bovine

https://doi.org/10.1021/acsnano.4c01672
ACS Nano XXXX, XXX, XXX−XXX

serum (FBS) and 1% GlutaMax (200 mM). Culture flasks were maintained in a humidified incubator at 37 °C with 5% CO_2. When at 80% of confluence, cells were enzymatically detached from the flasks with a 0.25% Trypsin-EDTA solution (Gibco ThermoFisher Scientific), plated on sterilized substrates (2×10^4 cells/coverslips), and left to grow for at least 24 h before the experiments. Prior to cell plating, a layer of fibronectin (2 μg/mL in PBS) was deposited on the sample surface and incubated for 1 h at 37 °C to promote cellular adhesion. HEK293T cells were incubated with BV-1 (1 μM, 5 min) in the culture media, and colocalization was evaluated at different time points (0, 1, 2, and 4 days after the single incubation). To evaluate the distribution of BV-1, the cell surface was labeled with CellMask (5 μM, 5 min). Live imaging was performed with an inverted confocal laser-scanning microscope (Nikon Instruments), and acquisitions were performed using an Olympus 60× oil objective. Cells were exposed to a 488 and 641 nm diode laser to excite BV-1 and CellMask, respectively. Colocalization of the two fluorescence signals was analyzed using ImageJ plugin JACoP. HEK293T cells were measured in the dark at room temperature (22−25 °C) in whole-cell configuration with freshly pulled glass pipettes (4−7 MΩ), filled with the following intracellular solution (mM): 12 KCl, 125 K Gluconate, 1 $MgCl_2$, 0.1 $CaCl_2$, 10 EGTA, 10 HEPES, and 10 ATP-Na_2 (pH 7.3 with KOH). The extracellular solution contained [mM] 135 NaCl, 5.4 KCl, 5 HEPES, 10 Glucose, 1.8 $CaCl_2$, and 1 $MgCl_2$ (pH 7.4 with NaOH). Standard patch-clamp recordings were performed using an Axopatch 200B with pClamp-10 software (Molecular Devices, San Jose, CA). Membrane currents were low pass filtered at 2 kHz and digitized with a sampling rate of 10 kHz using the Axon Digidata 1440A. A Spectra X Light Engine LED system (Lumencor) fiber-coupled to an Eclipse Ti inverted microscope (Nikon Instruments). The LED used as excitation light source was characterized by maximum emission wavelength at 474 nm. The illuminated spot on the sample has an area of 0.23 mm^2 and a photoexcitation density of 25 mW/mm^2, as measured at the output of the microscope objective. HEK293T cells were incubated with either vehicle (H_2O; 1%, v/v) or BV-1 (1 μM) for 5 min at room temperature and then washed twice with the extracellular solution to remove the unbound molecules. Current-clamp recordings were performed to study light-dependent membrane voltage modulation in isolated HEK293T cells. The light-induced depolarization was performed by holding the cell at its resting membrane potential ($I = 0$) and stimulating it with 1 Hz light pulses for 30 s for either 20 or 200 ms. Membrane potential was also recorded for another 30 s in the dark. The resulting depolarization was calculated with respect to the membrane potential value recorded for 1 s in the dark before the light stimulation. Modulation of membrane resistance was measured with current-clamp ramps injecting current from −120 to 40 pA in 300 ms upon 200 ms of light pulse stimulation. The membrane resistance was calculated as the corresponding slope of the recorded voltage traces. The protocol was repeated for 20 cycles with light pulses preceding the current-clamp ramp.

Light-Induced Membrane-Patch Perforation. To investigate the formation of pores on a membrane patch upon light stimulation, patch-clamp recordings were performed in a cell-attached configuration. Pipettes were filled with K-Aspartate internal solution containing (in mM) 130 K-Aspartate, 10 NaCl, and 10 HEPES (pH 7.3 with KOH). The patch pipettes were minimally front-filled with K-aspartate solution (from 1 to 5 s of tip immersion) and then backfilled with the same solution containing either BV-1 (diluted to a final concentration of 0.1 μM) or vehicle (H_2O; 0.1% v/v). We measured the transient capacitive currents by applying a 20 ms depolarizing voltage pulse of 5 mV from a holding potential of −70 mV in the absence of light stimulation (dark) or after successive cycles of illumination (200 ms, 3 mW/mm^2). The charge under the capacitive peak (Q_{peak}) was calculated by integrating the current traces, subtracting the charge passing through the patch membrane resistance (Q_{res}) from the total charge (Q_{tot}), obtained as the whole area. After giga-seal formation, the decrease in patch resistance after light-dependent perforation was calculated as the ratio between the voltage step and the amplitude of the steady-state current (I_{SS}).

Multielectrode Array Recordings in Blind Retinal Explants. Dystrophic retinas were dissected from the enucleated eyes of 12-month-old retinal degeneration 10 (rd10) mice carrying a spontaneous mutation of the rod-phosphodiesterase (PDE) gene, leading to a rod degeneration that starts around P18. Eyes were enucleated and transferred to a Petri dish with carboxygenated Ames medium (Sigma-Aldrich, Milano, Italy). The dissection procedure was performed in dim red light. After the removal of the cornea, iris, lens, and vitreous, each retina was dissected from the sclera, subdivided into pieces, and kept oxygenated in Ames medium. Each piece was incubated with either BV-1 (5 μM in Ames medium) or PBS (10% H_2O in Ames medium) for 30 min, subsequently washed in the fresh recording medium and positioned RGC side down onto a 60 electrodes MEA chip using the MEA1060-inv system (Multi Channel Systems MCS GmbH, Reutlingen, Germany). The light-evoked extracellular activity was obtained with a fiber-coupled Spectra X Light Engine LED system (Lumencor) peaking at 460 nm and fed to an inverted Eclipse Ti microscope (Nikon Instruments). The illumination spot covered an area of about 1 mm^2 at 0.5, 1, and 3 mW/mm^2. Data were acquired at 25 kHz and filtered between 200 Hz and 3 kHz. Spike detection was performed using MC Rack software (Multi Channel Systems). After the recording of a period of baseline firing in the dark, a 200 ms light pulse protocol administered at 1 Hz was employed at increasing power densities. Each power density protocol lasted 100 s (100 sweeps). Extracellular signals were high-pass filtered (200 Hz), and spike detection was set above 4.5-fold the standard deviation (SD) of the baseline. As a readout of light-induced firing rate modulation, we measured the spike count difference between 120−200 and 320−400 s time epochs after light onset and a corresponding window in the dark (1-s bins).

***In Vivo* Injection of BV-1 and Extracellular Recordings in the Primary Visual Cortex.** *BV-1 Injection in the Primary Visual Cortex (V1).* Naive C57BL/6 mice (Charles River) were anesthetized with xylazine (5 mg/kg) and ketamine (50 mg/kg) and placed in a stereotaxic frame (World Precision Instruments, Sarasota, FL) for surgery. Mice were injected in the binocular portion of V1 (OC1b; stereotaxic coordinates: 2.7 mm from the intersection between the sagittal and lambdoid sutures and ∼400 μm ventral to brain surface) with 1 μL of either BV-1 (500 μM in PBS) or vehicle (10% H_2O in PBS) using a 5-μL Hamilton syringe. A hole in the skull was drilled in correspondence of OC1b, the dura mater was gently removed after the exposure of the brain surface, and the injection was done at a rate of 500 nL/min with a nanoinjector (World Precision Instruments, Fl), keeping the needle in place for additional 10 min.

In Vivo Extracellular Recordings. Five minutes after the injection, anesthetized C57BL/6 mice were subjected to an extended craniotomy to perform *in vivo* recordings. After 60 min of recovery, an optic fiber cannula (200 μm in diameter; 50° normal to the skull; Doric Québec, Canada) and a glass micropipette (2−4 MΩ, filled with 3 M NaCl) were inserted in OC1b (350 μm depth) to reach the injected area. Pulsed light stimulation (430 nm LED, 40 mW/mm^2) was delivered 100−200 times at 1 Hz (200 ms), while prolonged light stimulation was subsequently administered for 30 s. Extracellular signals in response to stimulation were amplified and band-pass filtered (1−3000 Hz) by a NeuroLog system (Digitimer Ltd., Welwyn Garden City, U.K.) and finally digitized through a multifunction I/O device (NI USB-6251; National Instrument Co., Austin, TX). The same application software (MATLAB R2022b) was employed to drive both light stimulation and signal acquisition through a customized application. During the recordings, both eyes were maintained closed to avoid contamination by physiological visual signals from the retina. Mice reflexes and body temperature (36−37 °C) during the experiments were monitored and were stable. After recordings, mice were euthanized for imaging and immunohistochemical analysis.

Firing Rate Analysis. Extracellular signals were high-pass filtered (500 Hz), and spike detection was set above 5.5-fold the standard deviation (SD) of the baseline. As a readout of light-induced firing rate modulation, we measured the average ratio between the highest firing rate (10 s bins) after and before each stimulation protocol.

https://doi.org/10.1021/acsnano.4c01672
ACS Nano XXXX, XXX, XXX−XXX

Visual Cortex Immunohistochemistry. Mice were transcardially perfused with 4% paraformaldehyde (PFA) and then subjected to cervical dislocation. Brains were extracted, postfixed in 4% PFA in 0.1 M PBS overnight, and extensively washed in 0.1 M PBS. Brain sections of 40 μm thickness were obtained using a vibroslicer (Vibratome 5100 mz, Camden Instruments, Loughborough, U.K.), cryo-protected by equilibration with 30% sucrose, and incubated in freezing solution of 3% ethylene glycol, glycerol, 0.2 M phosphate buffer, Sigma) at −20 °C. For immunohistochemistry, brain sections were first incubated in blocking solution (0.1 M PBS, 10% bovine serum albumin, BSA, 1% Triton X-100) for 1 h at room temperature and then incubated overnight at 4 °C with rabbit anti-active caspase-3 (#AF835; 1:50 dilution; RD System). Alexa Fluor 647-conjugated secondary antibodies (Alexa 488-conjugated secondary antibodies hosted in goat, ThermoFisher Scientific) were diluted 1:100 and incubated at room temperature for 1 h. After counterstaining with Hoechst 33342, sections were let to dry and mounted with Mowiol. Brain sections were imaged with a SP8 confocal laser-scanning microscope (Leica Microsystems). The levels of induced cell death in the proximity of the BV-1 injection sites were quantified based on Hoechst 33342 and active caspase-3 staining within 20 μm z-stack volumes, acquired at 512 × 512 resolution and compared with the corresponding vehicle-injected areas. The percentage of cell death was calculated as the ratio between caspase-3 positive cells and the total number of Hoechst 33342-labeled cells in the stack.

Statistical Analysis. Data are shown as box plots or means ± SEMs with superimposed individual experimental points. The box plot elements are center line, median (Q2); square symbol, mean; box limits, 25th (Q1)-75th (Q3) percentiles; and whisker length is determined by the outermost data points within 3-fold the interquartile range (Q3−Q1). The normal distribution of data was assessed using the D'Agostino-Pearson's normality test. The F-test was used to compare the variance between the two sample groups. To compare two normally distributed sample groups, the unpaired or paired Student's t-test was used, as appropriate. To compare two sample groups that were not normally distributed, the Mann−Whitney's U-test and Wilcoxon test were used for unpaired and paired data, respectively. To compare more than two experimental groups, one- or two-way ANOVA/Šídák's tests and Kruskal−Wallis/Dunn's tests were used in the case of normal or non-normal distribution, respectively. A p-value <0.05 was considered significant. Statistical analysis was carried out using OriginPro-8 (OriginLab Corp., Northampton, MA) and Prism (GraphPad Software, Inc.).

ASSOCIATED CONTENT

Data Availability Statement

Raw data, simulation, and analysis are available from the authors upon reasonable request.

Supporting Information

The Supporting Information is available free of charge at https://pubs.acs.org/doi/10.1021/acsnano.4c01672.

Supplementary methods on the procedures for the synthesis of BV-1 (PDF) Donor−acceptor charge movement upon light stimulation (Figure S1); membrane voltage modulation 4 days after pulse incubation with BV-1 (Figure S2); distribution of BV-1 immersed in membrane bilayers in the dark and under light stimulation (Figure S3); light-triggered pore generation by BV-1 in Hek293 cells (Figure S4); the light-induced membrane depolarization induced by BV-1 is not reversible (Figure S5); BV-1 light-dependent modulation affects voltage-gated sodium channels (Figure S6); BV-1 light-dependent modulation affects voltage-gated potassium channels (Figure S7); light induces somatic swelling in neurons incubated with BV-1 (Figure S8); whole-cell recordings upon light-induced poration (Figure S9); lengths of BV-1 domains (Figure S10) (PDF)

HS-AFM movie of BV-1-induced changes of POPC/chol (1:1) membrane patches (Video 1) (MP4)

HS-AFM movie of BV-1 induced formation of membrane defects (Video 2) (MP4)

AUTHOR INFORMATION

Corresponding Authors

Mattia Lorenzo DiFrancesco − *IRCCS Ospedale Policlinico San Martino, 16132 Genova, Italy;* orcid.org/0000-0002-7511-4438; Email: mattia.difrancesco@iit.it

Pietro Baldelli − *Department of Experimental Medicine, University of Genova, 16132 Genova, Italy; IRCCS Ospedale Policlinico San Martino, 16132 Genova, Italy;* Email: pietro.baldelli@iit.it

Fabio Benfenati − *Center for Synaptic Neuroscience and Technology, Istituto Italiano di Tecnologia, 16132 Genova, Italy; IRCCS Ospedale Policlinico San Martino, 16132 Genova, Italy;* orcid.org/0000-0002-0653-8368; Email: fabio.benfenato@iit.it

Authors

Marlene E. Pfeffer − *Center for Synaptic Neuroscience and Technology, Istituto Italiano di Tecnologia, 16132 Genova, Italy; Department of Experimental Medicine, University of Genova, 16132 Genova, Italy*

Arin Marchesi − *WPI Nano Life Science Institute, Kanazawa University, Kanazawa 920-1192, Japan; Department of Experimental and Clinical Medicine, Università Politecnica delle Marche, 60126 Torrette di Ancona, Italy*

Filippo Galluzzi − *Center for Synaptic Neuroscience and Technology, Istituto Italiano di Tecnologia, 16132 Genova, Italy; The Open University Affiliated Research Centre at Istituto Italiano di Tecnologia (ARC@IIT), 16163 Genova, Italy*

Matteo Moschetta − *Center for Nano Science and Technology, Istituto Italiano di Tecnologia, 20134 Milano, Italy;* orcid.org/0000-0001-9679-3778

Andrea Rossini − *Center for Nano Science and Technology, Istituto Italiano di Tecnologia, 20134 Milano, Italy*

Simona Francia − *IRCCS Ospedale Policlinico San Martino, 16132 Genova, Italy*

Clemens M. Franz − *WPI Nano Life Science Institute, Kanazawa University, Kanazawa 920-1192, Japan*

Yulia Fok − *Aix-Marseille University, INSERM, DyNaMo, Turing Centre for Living Systems, 13288 Marseille Cedex 09, France*

Claire Valotteau − *Aix-Marseille University, INSERM, DyNaMo, Turing Centre for Living Systems, 13288 Marseille Cedex 09, France*

Giuseppe Maria Paternò − *Center for Nano Science and Technology, Istituto Italiano di Tecnologia, 20134 Milano, Italy; Department of Physics, Politecnico di Milano, 20133 Milan, Italy*

Lorena Redondo Morata − *Aix-Marseille University, INSERM, DyNaMo, Turing Centre for Living Systems, 13288 Marseille Cedex 09, France;* orcid.org/0000-0002-6254-8261

Francesca Vacca − *Center for Synaptic Neuroscience and Technology, Istituto Italiano di Tecnologia, 16132 Genova, Italy; IRCCS Ospedale Policlinico San Martino, 16132 Genova, Italy*

https://doi.org/10.1021/acsnano.4c01672
ACS Nano XXXX, XXX, XXX−XXX

Sara Mattiello − *Department of Material Science, Bicocca University, 20126 Milano, Italy;* orcid.org/0000-0002-2907-0964

Arianna Magni − *Center for Nano Science and Technology, Istituto Italiano di Tecnologia, 20134 Milano, Italy; Department of Physics, Politecnico di Milano, 20133 Milan, Italy*

Luca Maragliano − *Center for Synaptic Neuroscience and Technology, Istituto Italiano di Tecnologia, 16132 Genova, Italy; Department of Life and Environmental Sciences, Università Politecnica delle Marche, 60131 Ancona, Italy;* orcid.org/0000-0002-5705-6967

Luca Beverina − *Department of Material Science, Bicocca University, 20126 Milano, Italy;* orcid.org/0000-0002-6450-545X

Giuseppe Mattioli − *Istituto di Struttura della Materia, Consiglio Nazionale delle Ricerche (CNR-ISM), 00015 Monterotondo (RM), Italy;* orcid.org/0000-0001-6331-198X

Guglielmo Lanzani − *Center for Nano Science and Technology, Istituto Italiano di Tecnologia, 20134 Milano, Italy; Department of Physics, Politecnico di Milano, 20133 Milan, Italy;* orcid.org/0000-0002-2442-4495

Elisabetta Colombo − *Center for Synaptic Neuroscience and Technology, Istituto Italiano di Tecnologia, 16132 Genova, Italy; IRCCS Ospedale Policlinico San Martino, 16132 Genova, Italy*

Complete contact information is available at: https://pubs.acs.org/10.1021/acsnano.4c01672

Author Contributions

[§§]M.E.P., M.L.L.D., and F.B. contributed equally to this work.

Notes

The authors declare no competing financial interest.

ACKNOWLEDGMENTS

The authors are most thankful to Prof. Noriyuki Kodera for designing, developing, and integrating the blue-light irradiation system into the HS-AFM setup. The authors also thank R. Ciancio, I. Dallorto, A. Mehilli, R. Navone, and D. Moruzzo (Istituto Italiano di Tecnologia, Genova, Italy) for technical and administrative assistance. The study was supported by grants from H2020-MSCA-ITN 2019 "Entrain Vision" (project 861423 to F.B. and G.L.), Euronanomed3 (project Nanolight 2019-132 to F.B.), the Italian Ministry of Health (Ricerca Finalizzata GR-2021-12374630 to M.L.L.D. and RF-2021-12374404 to F.B.), Telethon Foundation Italy (grant GMR22T2013 to F.B.), Compagnia di San Paolo Trapezio (grant 118787 to F.B.), the Italian Ministry of University and Research (PRIN 2020WMSNBL to F.B.), and IRCCS Ospedale Policlinico San Martino Genova (Ricerca Corrente and 5 × 1000 grants to F.B. and E.C.). Support from the Japanese Ministry of Education, Culture, Sports, Science and Technology (World Premier International Research Center Initiative WPI) is also acknowledged. The authors gratefully acknowledge the HPC infrastructure and the Support Team at Fondazione Istituto Italiano di Tecnologia (Genova, Italy). M.E.P. is an MSCA PhD student supported by the Entrain Vision project; Y.F. is a PhD student supported by the French Agence Nationale de la Recherche (grant ANR-22-CE43-0017 MOWGLY), and C.V. work is supported by the French Center National de la Recherche Scientifique. The authors also acknowledge the CINECA award under the ISCRA initiative for the availability of high-performance computing resources and support.

REFERENCES

(1) Fenno, L.; Yizhar, O.; Deisseroth, K. The Development and Application of Optogenetics. *Annu. Rev. Neurosci.* **2011**, *34*, 389−412.
(2) Li, J.; Duan, H.; Pu, K. Nanotransducers for Near-Infrared Photoregulation in Biomedicine. *Adv. Mater.* **2019**, *31*, No. 1901607.
(3) Benfenati, F.; Lanzani, G.; Benfenati, F.; Lanzani, G. Clinical Translation of Nanoparticles for Neural Stimulation. *Nat. Rev. Mater.* **2021**, *6*, 1−4.
(4) Yang, X.; Mcglynn, E.; Das, R.; Paşca, S. P.; Cui, B.; Heidari, H. Nanotechnology Enables Novel Modalities for Neuromodulation. *Adv. Mater.* **2021**, *33*, No. 2103208.
(5) Carvalho-de-Souza, J. L.; Treger, J. S.; Dang, B.; Kent, S. B. H.; Pepperberg, D. R.; Bezanilla, F. Photosensitivity of Neurons Enabled by Cell-Targeted Gold Nanoparticles. *Neuron* **2015**, *86*, 207−217.
(6) Maya-Vetencourt, J. F.; Manfredi, G.; Mete, M.; Colombo, E.; Bramini, M.; Di Marco, S.; Shmal, D.; Mantero, G.; Dipalo, M.; Rocchi, A.; DiFrancesco, M. L.; Papaleo, E. D.; Russo, A.; Barsotti, J.; Eleftheriou, C.; Di Maria, F.; Cossu, V.; Piazza, F.; Emionite, L.; Ticconi, F.; Marini, C.; Sambuceti, G.; Pertile, G.; Lanzani, G.; Benfenati, F. Subretinally Injected Semiconducting Polymer Nanoparticles Rescue Vision in a Rat Model of Retinal Dystrophy. *Nat. Nanotechnol.* **2020**, *15*, 698−708.
(7) Francia, S.; Shmal, D.; Di Marco, S.; Chiaravalli, G.; Maya-Vetencourt, J. F.; Mantero, G.; Michetti, C.; Cupini, S.; Manfredi, G.; DiFrancesco, M. L.; Rocchi, A.; Perotto, S.; Attanasio, M.; Sacco, R.; Bisti, S.; Mete, M.; Pertile, G.; Lanzani, G.; Colombo, E.; Benfenati, F. Light-Induced Charge Generation in Polymeric Nanoparticles Restores Vision in Advanced-Stage Retinitis Pigmentosa Rats. *Nat. Commun.* **2022**, *13*, No. 3677.
(8) Wu, X.; Yang, F.; Cai, S.; Pu, K.; Hong, G. Nanotransducer-Enabled Deep-Brain Neuromodulation with NIR-II Light. *ACS Nano* **2023**, *17*, 7941−7952.
(9) Wu, X.; Jiang, Y.; Rommelfanger, N. J.; Yang, F.; Zhou, Q.; Yin, R.; Liu, J.; Cai, S.; Ren, W.; Shin, A.; Ong, K. S.; Pu, K.; Hong, G. Tether-Free Photothermal Deep-Brain Stimulation in Freely Behaving Mice via Wide-Field Illumination in the near-Infrared-II Window. *Nat. Biomed. Eng.* **2022**, *6*, 754−770.
(10) Bianco, A.; Perissinotto, S.; Garbugli, M.; Lanzani, G.; Bertarelli, C. Control of Optical Properties through Photochromism: A Promising Approach to Photonics. *Laser Photon. Rev.* **2011**, *5*, 711−736.
(11) Zhang, J.; Wang, J.; Tian, H. Taking Orders from Light: Progress in Photochromic Bio-Materials. *Mater. Horiz.* **2014**, *1* (2), 169−184.
(12) Gorostiza, P.; Isacoff, E. Optical Switches and Triggers for the Manipulation of Ion Channels and Pores. *Mol. Biosyst.* **2007**, *3*, 686−704.
(13) Fortin, D. L.; Banghart, M. R.; Dunn, T. W.; Borges, K.; Wagenaar, D. A.; Gaudry, Q.; Karakossian, M. H.; Otis, T. S.; Kristan, W. B.; Trauner, D.; Kramer, R. H. Photochemical Control of Endogenous Ion Channels and Cellular Excitability. *Nat Methods* **2008**, *5*, 331−338.
(14) Kramer, R. H.; Mourot, A.; Adesnik, H. Optogenetic Pharmacology for Control of Native Neuronal Signaling Proteins. *Nat. Neurosci.* **2013**, *16*, 816−823.
(15) Bléger, D.; Hecht, S. Visible-Light-Activated Molecular Switches. *Angew. Chem., Int. Ed.* **2015**, *54*, 11338−11349.
(16) Mourot, A.; Tochitsky, I.; Kramer, R. H. Light at the End of the Channel: Optical Manipulation of Intrinsic Neuronal Excitability with Chemical Photoswitches. *Front. Mol. Neurosci.* **2013**, *6*, 5.
(17) Mourot, A.; Kienzler, M. A.; Banghart, M. R.; Fehrentz, T.; Huber, F. M. E.; Stein, M.; Kramer, R. H.; Trauner, D. Tuning Photochromic Ion Channel Blockers. *ACS Chem. Neurosci.* **2011**, *2*, 536−543.

(18) DiFrancesco, M. L.; Lodola, F.; Colombo, E.; Maragliano, L.; Bramini, M.; Paternò, G. M.; Baldelli, P.; Serra, M. D.; Lunelli, L.; Marchioretto, M.; Grasselli, G.; Cimò, S.; Colella, L.; Fazzi, D.; Ortica, F.; Vurro, V.; Eleftheriou, C. G.; Shmal, D.; Maya-Vetencourt, J. F.; Bertarelli, C.; Lanzani, G.; Benfenati, F. Neuronal Firing Modulation by a Membrane-Targeted Photoswitch. *Nat. Nanotechnol.* **2020**, *15*, 296−306.
(19) Maria Paternò, G.; Colombo, E.; Vurro, V.; Lodola, F.; Cimò, S.; Sesti, V.; Molotokaite, E.; Bramini, M.; Ganzer, L.; Fazzi, D.; Benfenati, F.; Bertarelli, C.; Lanzani, G.; Paternò, G. M.; Vurro, V.; Lodola, F.; Molotokaite, E.; Lanzani, G.; Colombo, E.; Bramini, M.; Benfenati, F.; Benfenati IRCCS Ospedale Policlinico San Martino Largo Rosanna Benzi, F.; Vurro, I. V.; Ganzer, L.; Cimò, S.; Sesti, V.; Bertarelli, C.; Fazzi, D. Membrane Environment Enables Ultrafast Isomerization of Amphiphilic Azobenzene. *Adv. Sci.* **2020**, *7* (8), No. 1903241.
(20) Awasthi, N.; Kopec, W.; Wilkosz, N.; Jamróz, D.; Hub, J. S.; Zatorska, M.; Petka, R.; Nowakowska, M.; Kepczynski, M. Molecular Mechanism of Polycation-Induced Pore Formation in Biomembranes. *ACS Biomater. Sci. Eng.* **2019**, *5*, 780−794.
(21) Vandenabeele, P.; Bultynck, G.; Savvides, S. N. Pore-Forming Proteins as Drivers of Membrane Permeabilization in Cell Death Pathways. *Nat. Rev. Mol. Cell Biol.* **2023**, *24*, 312−333.
(22) García-López, V.; Chen, F.; Nilewski, L. G.; Duret, G.; Aliyan, A.; Kolomeisky, A. B.; Robinson, J. T.; Wang, G.; Pal, R.; Tour, J. M. Molecular Machines Open Cell Membranes. *Nature* **2017**, *548*, 567−572.
(23) García-López, V.; Liu, D.; Tour, J. M. Light-Activated Organic Molecular Motors and Their Applications. *Chem. Rev.* **2020**, *120*, 79−124.
(24) Schneckenburger, H. Laser-Assisted Optoporation of Cells and Tissues − a Mini-Review. *Biomed. Opt. Express.* **2019**, *10* (6), 2883−2888.
(25) Xiong, R.; Samal, S. K.; Demeester, J.; Skirtach, A. G.; De Smedt, S. C.; Braeckmans, K. Laser-Assisted Photoporation: Fundamentals, Technological Advances and Applications. *Adv. Phys. X* **2016**, *1*, 596−620.
(26) Bergeron, E.; Boutopoulos, C.; Martel, R.; Torres, A.; Rodriguez, C.; Niskanen, J.; Lebrun, J. J.; Winnik, F. M.; Sapieha, P.; Meunier, M. Cell-Specific Optoporation with near-Infrared Ultrafast Laser and Functionalized Gold Nanoparticles. *Nanoscale* **2015**, *7*, 17836−17847.
(27) Wang, W.; Wu, Z.; Lin, X.; Si, T.; He, Q. Gold-Nanoshell-Functionalized Polymer Nanoswimmer for Photomechanical Poration of Single-Cell Membrane. *J. Am. Chem. Soc.* **2019**, *141*, 6601−6608.
(28) Batabyal, S.; Kim, S.; Wright, W.; Mohanty, S. Laser-Assisted Targeted Gene Delivery to Degenerated Retina Improves Retinal Function. *J. Biophotonics* **2021**, *14*, No. e202000234.
(29) Hasanzadeh Kafshgari, M.; Agiotis, L.; Largillière, I.; Patskovsky, S.; Meunier, M. Antibody-Functionalized Gold Nanostar-Mediated On-Resonance Picosecond Laser Optoporation for Targeted Delivery of RNA Therapeutics. *Small* **2021**, *17*, No. 2007577.
(30) Pylaev, T. E.; Efremov, Y.; Avdeeva, E. S.; Antoshin, A. A.; Shpichka, A. I.; Khlebnikova, T. M.; Timashev, P.; Khlebtsov, N. G. Optoporation and Recovery of Living Cells under Au Nanoparticle Layer-Mediated NIR-Laser Irradiation. *ACS Appl. Nano Mater.* **2021**, *4*, 13206−13217.
(31) Dipalo, M.; Amin, H.; Lovato, L.; Moia, F.; Caprettini, V.; Messina, G. C.; Tantussi, F.; Berdondini, L.; De Angelis, F. Intracellular and Extracellular Recording of Spontaneous Action Potentials in Mammalian Neurons and Cardiac Cells with 3D Plasmonic Nanoelectrodes. *Nano Lett.* **2017**, *17*, 3932−3939.
(32) Watabe, N.; Ishida, Y.; Ochiai, A.; Tokuoka, Y.; Kawashima, N. Oxidation Decomposition of Unsaturated Fatty Acids by Singlet Oxygen in Phospholipid Bilayer Membranes. *J. Oleo Sci.* **2007**, *56*, 73−80.
(33) Magni, A.; Mattiello, S.; Beverina, L.; Mattioli, G.; Moschetta, M.; Zucchi, A.; Paternò, G. M.; Lanzani, G. A Membrane Intercalating Metal-Free Conjugated Organic Photosensitizer for Bacterial Photodynamic Inactivation. *Chem. Sci.* **2023**, *14*, 8196−8205.
(34) Beranova, L.; Cwiklik, L.; Jurkiewicz, P.; Hof, M.; Jungwirth, P. Oxidation Changes Physical Properties of Phospholipid Bilayers: Fluorescence Spectroscopy and Molecular Simulations. *Langmuir* **2010**, *26*, 6140−6144.
(35) Cwiklik, L.; Jungwirth, P. Massive Oxidation of Phospholipid Membranes Leads to Pore Creation and Bilayer Disintegration. *Chem. Phys. Lett.* **2010**, *486*, 99−103.
(36) Lis, M.; Wizert, A.; Przybylo, M.; Langner, M.; Swiatek, J.; Jungwirth, P.; Cwiklik, L. The Effect of Lipid Oxidation on the Water Permeability of Phospholipids Bilayers. *Phys. Chem. Chem. Phys.* **2011**, *13*, 17555−17563.
(37) Garcia-Manyes, S.; Domènech, Ò.; Sanz, F.; Montero, M. T.; Hernandez-Borrell, J. Atomic Force Microscopy and Force Spectroscopy Study of Langmuir-Blodgett Films Formed by Heteroacid Phospholipids of Biological Interest. *Biochim. Biophys. Acta, Biomembr.* **2007**, *1768*, 1190−1198.
(38) Khadka, N. K.; Timsina, R.; Rowe, E.; O'Dell, M.; Mainali, L. Mechanical Properties of the High Cholesterol-Containing Membrane: An AFM Study. *Biochim. Biophys. Acta, Biomembr.* **2021**, *1863*, No. 183625.
(39) Akaike, N.; Harata, N. Nystatin Perforated Patch Recording and Its Applications to Analyses of Intracellular Mechanisms. *Jpn. J. Physiol.* **1994**, *44*, 433−473.
(40) Ebihara, S.; Shirato, K.; Harata, N.; Akaike, N. Gramicidin-Perforated Patch Recording: GABA Response in Mammalian Neurones with Intact Intracellular Chloride. *J. Physiol.* **1995**, *484*, 77.
(41) Rae, J.; Cooper, K.; Gates, P.; Watsky, M. Low Access Resistance Perforated Patch Recordings Using Amphotericin B. *J. Neurosci. Methods* **1991**, *37*, 15−26.
(42) Gargini, C.; Terzibasi, E.; Mazzoni, F.; Strettoi, E. Retinal Organization in the Retinal Degeneration 10 (Rd10) Mutant Mouse: A Morphological and ERG Study. *J. Comp. Neurol.* **2007**, *500*, 222−238.
(43) Wang, T.; Reingruber, J.; Woodruff, M. L.; Majumder, A.; Camarena, A.; Artemyev, N. O.; Fain, G. L.; Chen, J. The PDE6Mutation in the Rd10 Retinal Degeneration Mouse Model Causes Protein Mislocalization and Instability and Promotes Cell Death through Increased Ion Influx. *J. Biol. Chem.* **2018**, *293*, 15332−15346.
(44) Do, M. T. H. Melanopsin and the Intrinsically Photosensitive Retinal Ganglion Cells: Biophysics to Behavior. *Neuron* **2019**, *104*, 205−226.
(45) Aranda, M. L.; Schmidt, T. M. Diversity of Intrinsically Photosensitive Retinal Ganglion Cells: Circuits and Functions. *Cell. Mol. Life Sci.* **2021**, *78*, 889−907.
(46) Panchal, R.; Smart, M.; Bowser, D.; Williams, D.; Petrou, S. Pore-Forming Proteins and Their Application in Biotechnology. *Curr. Pharm. Biotechnol.* **2002**, *3*, 99−115.
(47) Patil, S.; Raj, A. T. Commentary: Molecular Machines Open Cell Membranes. *Front. Oncol.* **2017**, *7*, 277 DOI: 10.3389/fonc.2017.00277.
(48) Broichhagen, J.; Schönberger, M.; Cork, S. C.; Frank, J. A.; Marchetti, P.; Bugliani, M.; Shapiro, A. M. J.; Trapp, S.; Rutter, G. A.; Hodson, D. J.; Trauner, D. Optical Control of Insulin Release Using a Photoswitchable Sulfonylurea. *Nat. Commun.* **2014**, *5* (1), No. 5116.
(49) Barber, D. M.; Schönberger, M.; Burgstaller, J.; Levitz, J.; Weaver, C. D.; Isacoff, E. Y.; Baier, H.; Trauner, D. Optical Control of Neuronal Activity Using a Light-Operated GIRK Channel Opener (LOGO). *Chem. Sci.* **2016**, *7*, 2347−2352.
(50) Rapozzi, V.; Beverina, L.; Salice, P.; Pagani, G. A.; Camerin, M.; Xodo, L. E. Photooxidation and Phototoxicity of π-Extended Squaraines. *J. Med. Chem.* **2010**, *53*, 2188−2196.
(51) Cohen, B. E. Amphotericin B Membrane Action: Role for Two Types of Ion Channels in Eliciting Cell Survival and Lethal Effects. *J. Membr. Biol.* **2010**, *238*, 1−20.

https://doi.org/10.1021/acsnano.4c01672
ACS Nano XXXX, XXX, XXX−XXX

(52) Kamiński, D. M. Recent Progress in the Study of the Interactions of Amphotericin B with Cholesterol and Ergosterol in Lipid Environments. *Eur. Biophys. J.* **2014**, *43*, 453−467.
(53) Kristanc, L.; Božič, B.; Jokhadar, Š. Z.; Dolenc, M. S.; Gomišček, G. The Pore-Forming Action of Polyenes: From Model Membranes to Living Organisms. *Biochim. Biophys. Acta, Biomembr.* **2019**, *1861*, 418−430.
(54) Lovisolo, D. Patch Clamp: The First Four Decades of a Technique That Revolutionized Electrophysiology and Beyond. *Rev. Physiol. Biochem. Pharmacol.* **2023**, *186*, 1−28.
(55) Marie, E.; Sagan, S.; Cribier, S.; Tribet, C. Amphiphilic Macromolecules on Cell Membranes: From Protective Layers to Controlled Permeabilization. *J. Membr. Biol.* **2014**, *247*, 861−881.
(56) Lv, C.; Gu, X.; Li, H.; Zhao, Y.; Yang, D.; Yu, W.; Han, D.; Li, J.; Tan, W. Molecular Transport through a Biomimetic DNA Channel on Live Cell Membranes. *ACS Nano* **2020**, *14*, 14616−14626.
(57) Kang, M.; Day, C. A.; Kenworthy, A. K.; DiBenedetto, E. Simplified Equation to Extract Diffusion Coefficients from Confocal FRAP Data. *Traffic* **2012**, *13*, 1589.
(58) Mingeot-Leclercq, M. P.; Deleu, M.; Brasseur, R.; Dufrêne, Y. F. Atomic Force Microscopy of Supported Lipid Bilayers. *Nat. Protoc.* **2008**, *3*, 1654−1659.
(59) Marchesi, A.; Umeda, K.; Komekawa, T.; Matsubara, T.; Flechsig, H.; Ando, T.; Watanabe, S.; Kodera, N.; Franz, C. M. An Ultra-Wide Scanner for Large-Area High-Speed Atomic Force Microscopy with Megapixel Resolution. *Sci. Rep.* **2021**, *11* (1), No. 13003.
(60) Marchesi, A.; Gao, X.; Adaixo, R.; Rheinberger, J.; Stahlberg, H.; Nimigean, C.; Scheuring, S. An Iris Diaphragm Mechanism to Gate a Cyclic Nucleotide-Gated Ion Channel. *Nat. Commun.* **2018**, *9* (1), No. 3978.
(61) Puppulin, L.; Kanayama, D.; Terasaka, N.; Sakai, K.; Kodera, N.; Umeda, K.; Sumino, A.; Marchesi, A.; Weilin, W.; Tanaka, H.; Fukuma, T.; Suga, H.; Matsumoto, K.; Shibata, M. Macrocyclic Peptide-Conjugated Tip for Fast and Selective Molecular Recognition Imaging by High-Speed Atomic Force Microscopy. *ACS Appl. Mater. Interfaces* **2021**, *13*, 54817−54829.
(62) Zuttion, F.; Redondo-Morata, L.; Marchesi, A.; Casuso, I.High-Resolution and High-Speed Atomic Force Microscope Imaging. In *Methods in Molecular Biology*; Springer: New York, 2018; Vol. *1814*, pp 181−200 DOI: 10.1007/978-1-4939-8591-3_11.
(63) López-Alonso, J.; Eroles, M.; Janel, S.; Berardi, M.; Pellequer, J.-L.; Dupres, V.; Lafont, F.; Rico, F. PyFMLab: Open-Source Software for Atomic Force Microscopy Microrheology Data Analysis. *Open Res. Eur.* **2023**, *3*, 187.
(64) Jo, S.; Kim, T.; Iyer, V. G.; Im, W. CHARMM-GUI: A Web-Based Graphical User Interface for CHARMM. *J. Comput. Chem.* **2008**, *29*, 1859−1865.
(65) Phillips, J. C.; Braun, R.; Wang, W.; Gumbart, J.; Tajkhorshid, E.; Villa, E.; Chipot, C.; Skeel, R. D.; Kalé, L.; Schulten, K. Scalable Molecular Dynamics with NAMD. *J. Comput. Chem.* **2005**, *26*, 1781−1802.
(66) Huang, J.; Mackerell, A. D. CHARMM36 All-Atom Additive Protein Force Field: Validation Based on Comparison to NMR Data. *J. Comput. Chem.* **2013**, *34*, 2135−2145.
(67) Vanommeslaeghe, K.; Hatcher, E.; Acharya, C.; Kundu, S.; Zhong, S.; Shim, J.; Darian, E.; Guvench, O.; Lopes, P.; Vorobyov, I.; Mackerell, A. D. CHARMM General Force Field: A Force Field for Drug-like Molecules Compatible with the CHARMM All-Atom Additive Biological Force Fields. *J. Comput. Chem.* **2010**, *31*, 671−690.
(68) Ryckaert, J. P.; Ciccotti, G.; Berendsen, H. J. C. Numerical Integration of the Cartesian Equations of Motion of a System with Constraints: Molecular Dynamics of n-Alkanes. *J. Comput. Phys.* **1977**, *23*, 327−341.
(69) Darden, T.; York, D.; Pedersen, L. Particle Mesh Ewald: An N·log(N) Method for Ewald Sums in Large Systems. *J. Chem. Phys.* **1993**, *98*, 10089−10092.
(70) Feng, S.; Park, S.; Choi, Y. K.; Im, W. CHARMM-GUI Membrane Builder: Past, Current, and Future Developments and Applications. *J. Chem. Theory Comput* **2023**, *19*, 2161−2185.
(71) Neese, F. Software Update: The ORCA Program System, Version 4.0. *Wiley Interdiscip. Rev.: Comput. Mol. Sci.* **2018**, *8*, No. e1327.
(72) Neese, F. The ORCA Program System. *Wiley Interdiscip. Rev.: Comput. Mol. Sci.* **2012**, *2*, 73−78.
(73) Zhang, Y.; Yang, W. Comment on "Generalized Gradient Approximation Made Simple. *Phys. Rev. Lett.* **1998**, *80*, 890.
(74) Grimme, S.; Antony, J.; Ehrlich, S.; Krieg, H. A Consistent and Accurate Ab Initio Parametrization of Density Functional Dispersion Correction (DFT-D) for the 94 Elements H-Pu. *J. Chem. Phys.* **2010**, *132*, No. 154104, DOI: 10.1063/1.3382344.
(75) Schäfer, A.; Horn, H.; Ahlrichs, R. Fully Optimized Contracted Gaussian Basis Sets for Atoms Li to Kr. *J. Chem. Phys.* **1992**, *97*, 2571−2577.
(76) Cammi, R.; Mennucci, B.; Tomasi, J. Fast Evaluation of Geometries and Properties of Excited Molecules in Solution: A Tamm-Dancoff Model with Application to 4-Dimethylaminobenzonitrile. *J. Phys. Chem. A* **2000**, *104*, 5631−5637.

https://doi.org/10.1021/acsnano.4c01672
ACS Nano XXXX, XXX, XXX−XXX